

Three-dimensional localization of neurons in cortical tetrode recordings

Ferenc Mechler, Jonathan D. Victor, Ifije Ohiorhenuan, Anita M. Schmid and Qin Hu

J Neurophysiol 106:828-848, 2011. First published 25 May 2011; doi:10.1152/jn.00515.2010

You might find this additional info useful...

Supplemental material for this article can be found at:

<http://jn.physiology.org/content/suppl/2011/06/13/jn.00515.2010.DC1.html>

This article cites 81 articles, 31 of which can be accessed free at:

<http://jn.physiology.org/content/106/2/828.full.html#ref-list-1>

Updated information and services including high resolution figures, can be found at:

<http://jn.physiology.org/content/106/2/828.full.html>

Additional material and information about *Journal of Neurophysiology* can be found at:

<http://www.the-aps.org/publications/jn>

This information is current as of September 6, 2011.

Three-dimensional localization of neurons in cortical tetrode recordings

Ferenc Mechler, Jonathan D. Victor, Ifije Ohiorhenuan, Anita M. Schmid, and Qin Hu

Department of Neurology and Neuroscience, Medical College of Cornell University, New York, New York

Submitted 8 June 2010; accepted in final form 23 May 2011

Mechler F, Victor JD, Ohiorhenuan I, Schmid AM, Hu Q. Three-dimensional localization of neurons in cortical tetrode recordings. *J Neurophysiol* 106: 828–848, 2011. First published May 25, 2011; doi:10.1152/jn.00515.2010.—The recording radius and spatial selectivity of an extracellular probe are important for interpreting neurophysiological recordings but are rarely measured. Moreover, an analysis of the recording biophysics of multisite probes (e.g., tetrodes) can provide for source characterization and localization of spiking single units, but this capability has remained largely unexploited. Here we address both issues quantitatively. Advancing a tetrode ($\approx 40\text{-}\mu\text{m}$ contact separation, tetrahedral geometry) in 5- to 10- μm steps, we repeatedly recorded extracellular action potentials (EAPs) of single neurons in the visual cortex. Using measured spatial variation of EAPs, the tetrodes' measured geometry, and a volume conductor model of the cortical tissue, we solved the inverse problem of estimating the location and the size of the equivalent dipole model of the spike generator associated with each neuron. Half of the 61 visual neurons were localized within a radius of $\approx 100\ \mu\text{m}$ and 95% within $\approx 130\ \mu\text{m}$ around the tetrode tip (i.e., a large fraction was much further than previously thought). Because of the combined angular sensitivity of the tetrode's leads, location uncertainty was less than one-half the cell's distance. We quantified the spatial dependence of the probability of cell isolation, the isolated fraction, and the dependence of the recording radius on probe size and equivalent dipole size. We also reconstructed the spatial configuration of sets of simultaneously recorded neurons to demonstrate the potential use of 3D dipole localization for functional anatomy. Finally, we found that the dipole moment vector, surprisingly, tended to point toward the probe, leading to the interpretation that the equivalent dipole represents a "local lobe" of the dendritic arbor.

recording radius; extracellular action potential; multisite recording; inverse problem; equivalent dipole; lead field theory

MULTICONTACT RECORDINGS HAVE HIGH YIELD (Blanche et al. 2005; Csicsvari et al. 2003; Eckhorn and Thomas 1993; Gray et al. 1995; McNaughton et al. 1983) and improved accuracy of single-unit isolation (Harris et al. 2000; Schmitzer-Torbert et al. 2005). As models (Gold et al. 2006; Moffitt and McIntyre 2005; Pettersen and Einevoll 2008) predict and experiments (Buzsaki and Kandel 1998; Drake et al. 1988; Henze et al. 2000) show, the shape and size of the extracellular action potential (EAP) waveform depends on the relative position of cell and probe. Thus, these recordings carry spatial information about spike sources that is not available in single electrode records. However, this spatial information is typically not exploited, because extracting it requires solution of an inverse problem, deducing the position and the size of the current source of a spiking neuron from measurements of its EAP at multiple locations.

Address for reprint requests and other correspondence: F. Mechler, Dept. of Neurology and Neuroscience, Medical College of Cornell University, 1300 York Ave., New York, NY 10065-4805 (e-mail: fmechler@med.cornell.edu).

Here, we solve this inverse problem by modeling the spiking neuron with a single current dipole. The choice of a dipole model rests on reasoning presented in detail in a companion paper and its supplemental material (Mechler and Victor 2011). Briefly, although the membrane currents of a spiking neuron constitute a genuinely distributed current source, the resulting extracellular field is well approximated by that of a dipole beyond a minimum distance and throughout the typical cell-probe distances. The dipole approximation breaks down at distances shorter than 30–50 μm from the cell, but it accurately localizes the source provided that the cell-probe separation is greater than this minimum. Supporting evidence for this [detailed in the companion paper (Mechler and Victor 2011)] comes from extensive reanalysis of published data from other laboratories and computer simulations. The monopole, with four parameters (1 for intensity and 3 for the spatial coordinates; 2 fewer than the 6 parameters of the dipole), is the simplest possible source model, and it has been the most frequently used alternative of the dipole in neuron localization (Chelaru and Jog 2005; Lee et al. 2007; Somogyvari et al. 2005). However, it has a critical albeit hitherto not-well-recognized flaw; it seriously underestimates the source distance at typical cell-probe distances (see DISCUSSION; also see companion paper and its supplemental material from Mechler and Victor 2011). All other alternatives to the dipole will necessarily have higher-order multipole contributions and thus will have the disadvantage of requiring significantly more data to constrain.

Tetrodes of nonplanar contact configuration (such as the conical Thomas tetrodes), unlike some other single-cell recording probes (e.g., linear or some planar arrays), have full spherical sensitivity and thus offer spatially unconstrained data to which any model-based localization method could be applied and tested [note that spherical sensitivity is a property of the probe; methods of cell localization that use multipole source models (monopole, dipole, etc.) will retain the spherical sensitivity of the probe but will differ in radial accuracy]. Here, we apply our dipole localization technique to identify the 3D position and source magnitude of more than 60 neurons. The dipole model explained 95% of the power in the EAP data. From this population data, we derive an estimate of the recording radius of a tetrode, estimate the fraction of neurons within its recording volume that it isolates, measure the cortical distribution of single neuron current source strength, and reconstruct the spatial configuration of local neuron ensembles.

Our tetrodes (Thomas Recording) are similar to those that many laboratories use to record from single units in cortex. Specifically for these probes, we find a recording radius of $\approx 100\ \mu\text{m}$ defined by the volume enclosing one-half of the recorded neurons ($\approx 130\ \mu\text{m}$ for the 95th percentile). Within this recording volume, a single neuron's location can be

determined to within a sphere of radius $\approx 50 \mu\text{m}$ if the tetrode is gradually “stepped” through cortex. We estimate that the isolated fraction of all neurons present within the recording volume is only about 1% or smaller. We find the measured distribution of the dipole strength and orientation consistent with a novel recognition that the equivalent dipole corresponds to a “local lobe,” i.e., the lobe on the arbor of apical and major basal dendrites nearest to the probe. This interpretation of the equivalent source is rooted in cellular morphology and biophysics and accounts for a diverse set of physiological observations.

The localization capacity inherent in the “stepping tetrode” or static polytrode technique is potentially of substantial physiological importance. On the probed scale ($\approx 100 \mu\text{m}$), the functional microarchitecture of cortex consists of local ensembles within cortical layers defined by shared input (Callaway 1998; Yoshimura et al. 2005) and, across layers, of functionally related neurons linked into perpendicular microcolumns (Mountcastle 2003). How this organization determines local anatomic and physiological scatter is a subject of sustained interest (DeAngelis et al. 1999; Gallant et al. 1996; Hetherington and Swindale 1999; Hubel and Wiesel 1974; Ohki et al. 2005; Yao and Li 2002; Yen et al. 2007), and addressing this question demands tools with access to all cortical layers with high spatial resolution and the ability to capture neuronal dynamics on the ms scale. Tetrode recordings made with the stepping method can fill this niche by making the high-resolution reconstruction of the 3D spatial configuration of local ensembles feasible, a novel complement to routine application of these probes to the physiological characterization of single units.

METHODS

Physiological Preparation

The experimental procedures were conducted in accordance with the National Institutes of Health’s guidelines for the care and experimental use of animals and under an approved protocol from the Weill Cornell Medical College Institutional Animal Care and Use Committee. These experiments (“stepping”: intentionally moving the recording tetrode in 5- to 15- μm steps) were interleaved between a larger battery of experiments devoted to receptive field analysis that were carried out with standard tetrode recording (Mechler et al. 2007; Victor et al. 2006). The details of these preparations were described in full there. Briefly, standard acute experiments were carried out in the visual cortex of one adult male cat (3 kg) and two adult male macaque monkeys (4–6 kg). Via surgery under initial gas anesthesia (1% isoflurane), the animal was fitted with an endotracheal tube for mechanical ventilation, a femoral arterial blood pressure probe, and femoral venous catheters for delivery of anesthetics [a mixture of propofol (Propofol; 2–10 $\text{mg}\cdot\text{kg}^{-1}\cdot\text{h}^{-1}$) and sufentanil citrate (Sufenta, 0.05–0.5 $\mu\text{g}\cdot\text{kg}^{-1}\cdot\text{h}^{-1}$)] and a paralytic (vecuronium bromide, 1–2 mg/h). EKG, heart rate, blood pressure, end-tidal CO_2 , rectal temperature, urine output, and EEG were continuously monitored throughout the experiment, and body temperature was maintained in the physiological range via a temperature-controlled heating blanket.

Recording

A 10- to 15-mm-diameter craniotomy and a smaller, ≈ 3 -mm-diameter durotomy was made to expose the visual cortex (either the striate or the early extrastriate cortices). In each animal, one to three

recording tetrodes were placed on parallel tracks, spaced $>300 \mu\text{m}$ apart. An agarose-filled chamber surrounding the tetrodes insured mechanical stability of recording. The headstage-amplified analog signal from the four channels of the tetrodes (Minimatrix system; Thomas Recording) was amplified, filtered (300- to 9,000-Hz pass-band), and digitally sampled at 22,222 Hz (Cheetah data acquisition system; Neuralynx). On each tetrode separately, a negative-going threshold-crossing event on any of the four channels of the tetrode (referenced to a skull screw) triggered the storage of 32 sample points/channel (1.4 ms) of the EAP waveform on each of the four channels, beginning eight samples (350 μs) before the peak potential. Thresholds on each channel were set low enough to prevent missing spikes from candidate single units, even at the cost of permitting recording spike events from low signal-to-noise ratio (S/N) multiunit sources. Because the triggering mode of the acquisition software was limited to one polarity of voltage departures (either rising through a positive value or falling through a negative value), we were forced to choose between recording extracellular action potentials whose dominant features were positive-going or negative-going peaks. We chose the latter because negative-peaked EAPs are encountered most frequently. [Due to the layout of dendritic line source configurations in pyramidal neurons, positive-peaked EAPs are weaker and spatially confined to the close proximity of major primary dendrites (Rall 1962), making them harder to detect by the electrode.]

Figure 1 illustrates the main aspects of the methods, data collection, tetrode stepping, and spike preprocessing. Note that in this article we use the convention of plotting action potentials with polarity inversion (e.g., negative up).

Spatial Sampling of EAP in Tetrode-Stepping Experiments

We used the tetrode with a quantitative stepping method similar in spirit to the approach pioneered by Rosenthal et al. (1966) for a single electrode. The visually stimulated spike activity of a local group of isolated single neurons was recorded repeatedly at incremental depths along the tetrode penetration. The tetrode could be advanced to a specified position along its track with 1- μm accuracy under the computer control of the microdrive (Thomas Recording) (Eckhorn and Thomas 1993).

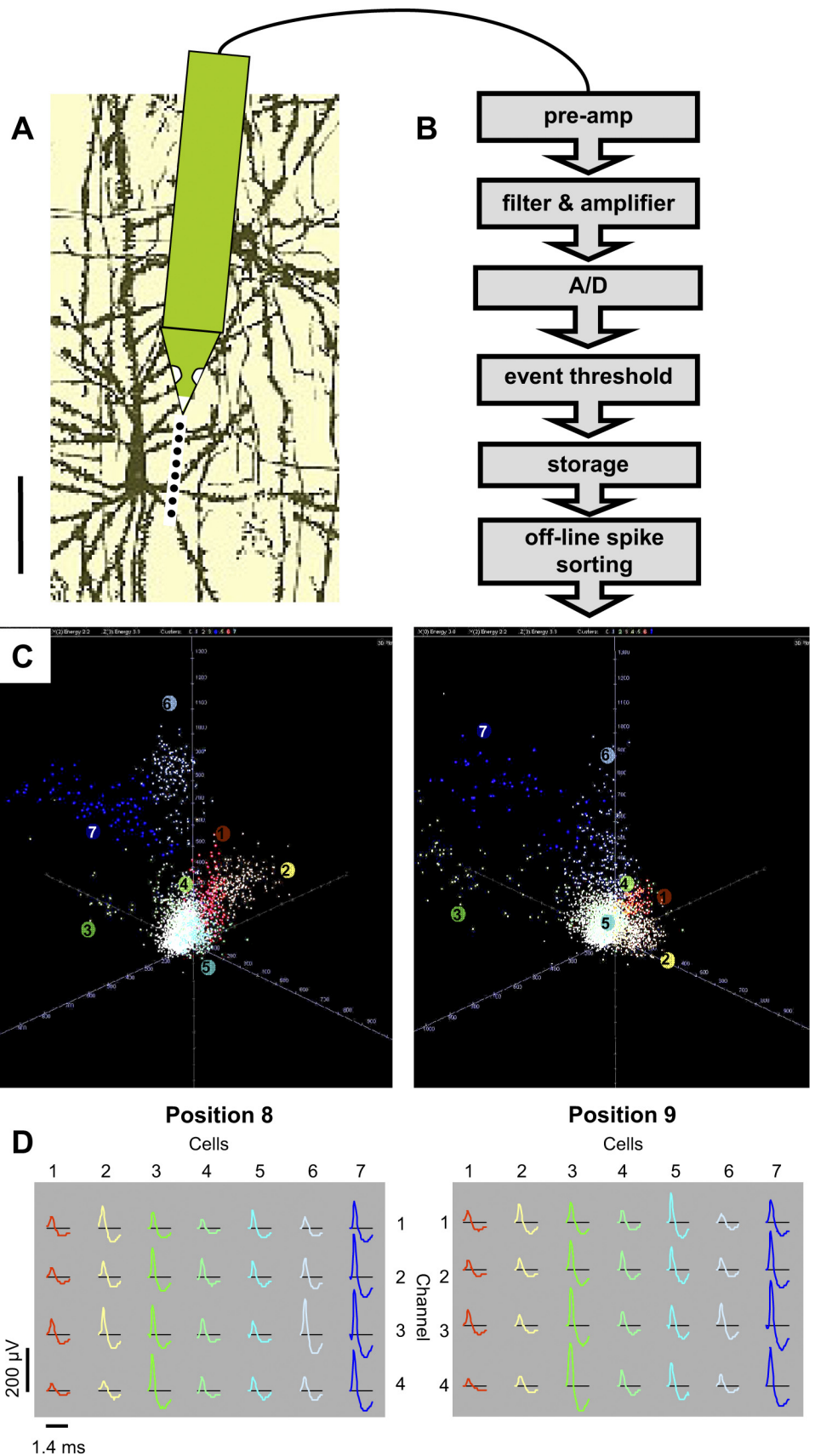
A step consisted of advancing the tetrode very slowly ($\approx 1 \mu\text{m}/\text{s}$) for a specified step size (fixed for the entire experiment). A 1- to 3-min interval followed each step to allow for tissue relaxation before the recording of visually stimulated spiking at the new recording position. Presented for a period of 2–4 min, the visual stimulus consisted of computer-controlled drifting gratings, in which orientation or spatial frequency was randomized, or a hand-controlled grating or laser spot that is typically used during the “searching” mode of cortical visual neurophysiological experiments.

An experiment lasted ~ 1 h and consisted of nine to 18 cycles of the above step-wait-record sequence. Based on pilot experiments, we chose a step size of 5–10 μm and chose the number of steps to cover a total distance of $90 \pm 10 \mu\text{m}$ along the recording track. With these choices we were able to collect and isolate spikes from single units at several consecutive recording positions (typically 3–6 steps; 50- μm median span), and the spatial variation in spike shape over that track segment was sufficiently large to allow for fitting the model dipole.

Figure 2A shows a typical data set (the spike emerged in *step 1* and was held through *step 6*; only these steps are shown). Note that at the central contact (*channel 0*, the channel with the 2nd largest signal) the waveform has maximal peak amplitude at *step 1* (at 875 μm), two or more steps ahead of the other channels (*channel 2*, with the largest signal, peaks second at 895 μm). This is not surprising given the geometry of the tetrode; the central contact emerges from the tip, whereas the other contacts (*leads 1, 2, and 3*) emerge from the sides of the cone (as diagrammed in Fig. 1A and Fig. 3).

The example shown is typical of the recordings. The 95% confidence limit on the mean waveform was very low, $\pm 2 \mu\text{V}$ on average,

Fig. 1. Overview of the tetrode-stepping experiments. *A*: a cartoon of the Thomas tetrode is superimposed on a scale-preserving (but cropped) mosaic image of neocortical neurons (used here solely for the purpose of giving a sense of the relative spatial scale of the probe and histology). The separation ($\approx 30 \mu\text{m}$) of the 4 contacts on the conical tetrode tip is comparable with the typical separation of cell bodies in neocortex. The dots along the line of penetration mark the recording sites at successive steps. The vertical scale bar represents $100 \mu\text{m}$. *B*: the analog spike waveforms are amplified, filtered, digitized, and stored on a computer for offline analysis. *C*: spike sorting consists of a step-by-step clustering and linking of single-unit data across steps. The images are the 3D visualization of spike feature space (here, waveform energy on 3 of the 4 tetrode channels) in 2 consecutive steps. The step-by-step change of cluster configuration is a result of the change in spike waveforms. Monitoring the movement of clusters in feature space helps trace the identity of candidate single units (indicated by cluster color and label) from 1 step to the next. *D*: the mean spike waveforms on all 4 tetrode channels (rows) for each single unit (columns) identified in the 2 steps shown in *C*. Bars indicate the scale of time and voltages. The 95% confidence limits on the mean voltages were around $\pm 2 \mu\text{V}$ (not shown). Note that upward deflections represent negative extracellular action potentials (EAPs). Mosaic image of Golgi-stained neurons of human motor cortex is reproduced, with permission, from Marin-Padilla 1990 © (MIT Press).



because it is an average of several dozens to several thousands of spike events per neuron at each step. The mean (range) noise level was $21 \mu\text{V}$ ($12\text{--}35 \mu\text{V}$). The spatial minimum of the peak EAP amplitude, defined for the same tetrode channel that registered the overall maximum peak, averaged $91 \mu\text{V}$ ($25\text{--}313 \mu\text{V}$). This spatial “mini-max” EAP amplitude indicates the effective criterion for single-unit isolation in our recording. These values are similar to what other laboratories reported for their tetrode or polytodes (Blanche et al. 2005; Henze et al. 2000; Musial et al. 2002).

Spike Preprocessing

The recorded extracellular action potential waveforms were pre-processed offline for further analysis in a three-stage procedure, as

described below. No neurons were recorded simultaneously on more than one tetrode, so each tetrode’s data were handled independently.

The first stage was semiautomated spike sorting. This was carried out separately at each stepped position. Spike clusters corresponding to candidate single units were identified by using the commercial software SpikeSort-3D (Neuralynx), which combines an efficient automated spike-clustering algorithm (Klustakwik; by Dr. Ken Harris) with a versatile graphic user interface. The algorithm works in multidimensional “feature spaces;” we typically used waveform energy or peak voltages on each channel as coordinates. The initial automated selection of candidate spike clusters was conservative (tending to create multiple clusters from spikes from the same source rather than a single cluster of spikes from different sources) and yielded more clusters than were eventually accepted as single units. To create final clusters, these candidate clusters were manually fused, and noisy clusters were eliminated. Our criteria to combine two clusters were that their corresponding waveforms were scaled versions of similarly shaped spikes, that their projections into “feature spaces” were continuous, and that the events in the fused cluster passed a 1.3-ms absolute refractory period criterion.

In the second stage, cluster identity was traced through all tetrode steps. This user input-dependent process was aided by the visualization of the multidimensional spike “feature space.” Figure 1C illustrates typical cluster movements in this space across a step of $10 \mu\text{m}$. Because the step size was kept small ($\leq 10 \mu\text{m}$), cluster configuration in feature space typically changed in an orderly fashion and provided a useful aid in tracing the same unit across steps. The relative size of clusters (in terms of spike counts) was a similarly useful characteristic of unit identity. However, challenges were presented by occasional large abrupt changes in cluster configuration or by the appearance or disappearance of clusters across a pair of consecutive recording positions. Because of this, correlations in waveform shape (or a difference-of-waveform norm) could not be used as the sole indicator of cluster identity. Consequently, although automated tracking of clusters across discrete recording positions would have considerably improved the efficacy of our dipole localization procedure, existing automated cluster linking methods (Emondi et al. 2004; Wolf and Burdick 2009) would not have sufficed. Additionally, the candidate set of clusters to be linked had to pass a test concerning the noise covariance; the noise covariance (across the 4 channels) had to be similar at each tetrode position. This criterion was included to ensure that there was no new “noise source” (e.g., a new unit included in the cluster) as the tetrode progressed.

Finally, to obtain the waveforms used for dipole localization, waveform samples were interpolated (cubic spline), aligned to peak time (center of mass across the 4 tetrode channels), and averaged separately for each cluster at each recording site.

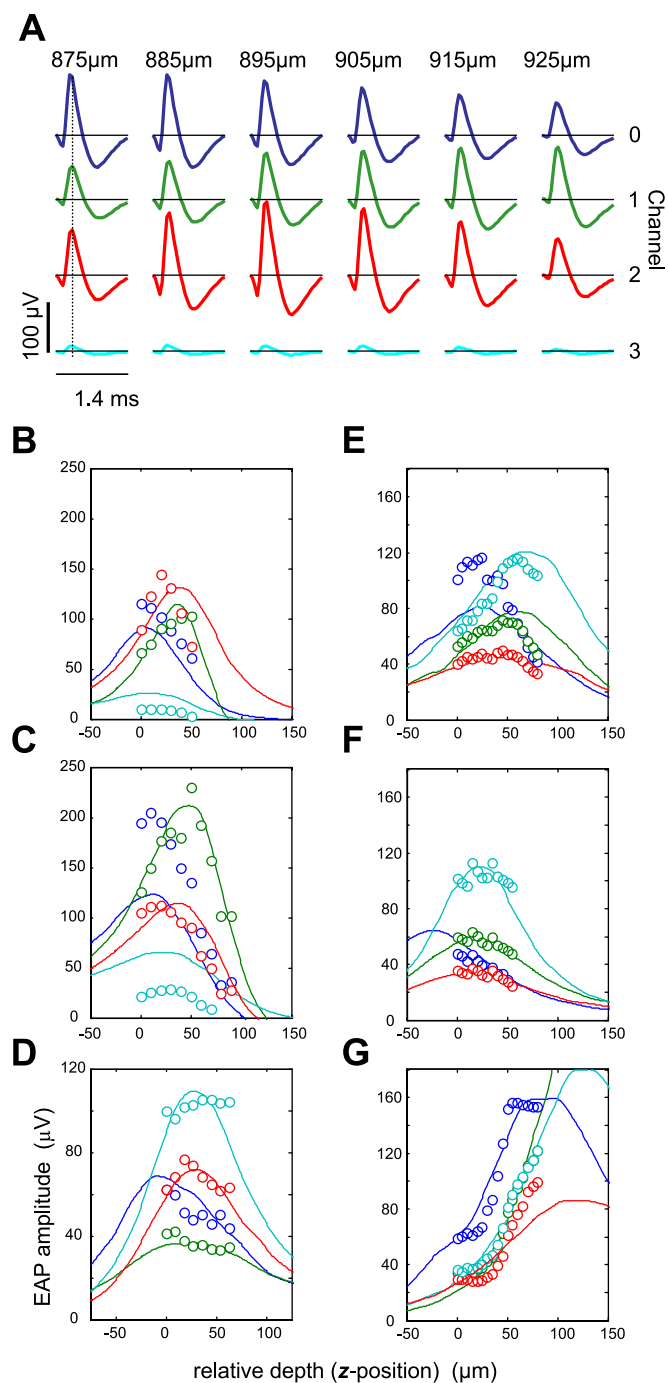


Fig. 2. A: typical data set collected by a stepping tetrode (a single unit in macaque V4, L53c02t2 Unit 2). The spike waveforms (average of 900–1,400 spikes/step) registered by the 4 channels (rows) of the tetrode are shown in separate columns for each of the 6 equidistant recording positions (top). Waveforms were interpolated from 32 digital samples. Upward deflections represent negative EAPs. The 95% confidence limit ($\pm 2 \mu\text{V}$) on the spike waveforms was smaller than the displayed line thickness. B: the spatial EAP amplitude at a fixed sample time (0.35 ms ; vertical line in A), plotted in different color for each channel as a function of penetration depth relative to the initial tetrode position. The continuous lines are the fits by the optimal dipole source model. C–G: 5 more cells with similar data and the optimal dipole fits. The macaque V4 cell in C was isolated in the same track segment as the example in B. The cat V1 cells in E–G were also isolated in the same track segment. The fitting error in C was twice the sample average and not typical (the model fits had larger errors for only 5 of the 61 cells); the other cells show the typical range (fractional root mean squared error < 0.05). The recovered cell probe distances in these 6 examples span the 60- to 120- μm range, also typical of the entire sample. The R-Z coordinates recovered for these cells are given in the legend to Fig. 4.

Dipole Characterization

A full treatment of our model-based approach to localizing a spiking single unit from a set of spatially sampled extracellular action potentials is given in a separate paper (Mechler and Victor 2011); here, we present its main features.

The system consists of a volume conductor model of a block of cortical tissue, a single-point dipole current source model of a spiking neuron, and a multicontact probe (tetrode or polytrode) with faithfully reconstructed geometry located somewhere within the volume conductor. The forward transformation that solves the potential of a known dipole is linear. Given the boundary conditions (zero potential at the sides and bottom of the volume conductor, insulation at its surface toward the dura and on its shared surfaces with the probe, except at the contacts), the sought quantity, the electrical potential at the contacts of the recording probe, has a unique value that can be obtained by numerical integration. Our interest is in the “inverse problem,” deducing the parameters (size and spatial coordinates) of the source from a set of voltage measurements. As is well known, at least since Helmholtz (1853), inverse problems are ill-posed (and often nonlinear), and the solutions are necessarily conditional (and approximate) and require special methods of further constraining—regularizing—the problem. For this reason, the source model is customarily restricted to a single dipole in biological (e.g., EKG, EEG) source imaging; higher moments are doubtless present, but including them in the source model yields diminishing returns. Because of the presence of noise in the data and the approximation in the model, predictions are not expected to be an exact account of the data; solutions are instead sought via optimizing an objective function that represents a tradeoff between precisely accounting for the data and a reasonable (i.e., low-magnitude) source.

Framing the problem as dipole characterization has the advantage that it is separable into a linear optimization of the dipole moment and a nonlinear optimization of spatial coordinates on the space of the linear solutions. Thus, our overall approach is to consider a large number of candidate dipole locations (see below) and for each candidate location to determine the optimal dipole moment. The latter is a linear problem and can be solved exactly. The solution is obtained by a matrix operation that involves the “lead fields” of the tetrode. These fields, one for each contact (“lead”) of the probe, defined at every point in the volume conductor, conveniently summarize the properties of the tissue + probe system. Lead fields are the forward solution of a “reciprocal” problem; they are the fields that result from injection of current through the probe contacts. We solved the lead fields numerically using the finite element method on an adaptive discrete mesh and interpolated them on a regular cylindrical grid.

To solve the nonlinear part of the problem, i.e., to localize the dipole on a cylindrical grid, we applied the L-curve regularization method (Hansen and Oleary 1993), a variant of Tikhonov regularization, to optimize model error while minimizing dipole size. The method is helpful to constrain the solution of ill-posed problems where the error as a function of model parameters has a plateau (as in the foot of an “L”) rather than a clear-cut minimum (as in a “V”).

The reason that a regularization approach is necessary and that a more straightforward least-squares approach will fail can be summarized as follows [see the companion paper (Mechler and Victor 2011) for further details]. There are two sources of error in the fit: error because there is noise in the measurements themselves and error because the source model, a dipole, is only approximate. Simply minimizing total error can lead to severe biases in localization. This is because the minimization will choose a position for the dipole at which measurement error and model error happen to cancel; i.e., the error in the model is fitting the noise in the measurement. To avoid this problem, we make use of the fact that this undesired behavior typically occurs for a dipole that is positioned at an unreasonably large distance (several hundred microns) and has a nonphysiological size. Put another way, we can prevent the model from fitting noise by

keeping the model dipole small. This is formalized by the regularization method mentioned above.

The credentials of this strategy are a focus of the companion paper, and we summarize conclusions of that analysis here (Mechler and Victor 2011). Up to a certain dipole size, the fitting error (residual) is very sensitive to dipole parameters; the residual steeply decreases with increasing dipole size. In this model-limited range, small adjustments in the dipole vector location, direction, and size result in a systematic and meaningful improvement in the ability of the model to account for the data. But above that certain dipole size, the typical gain in error reduction is diminished and no longer smooth. This is the regime in which model error dominates the residual (signifying the limitations of the dipole class), but dipole parameters become very sensitive to noise, and solutions are not stable. Correspondingly, in this regime the residual as a function of dipole size is rather flat but has odd minima at isolated points, as is typical for solutions of discrete inverse problems. Tikhonov regularization, by trading off error norm with dipole norm, offers a disciplined and robust way to constrain the solution to be meaningful. The optimal dipole is thus defined as the largest dipole in the smooth model-limited regime (or the smallest dipole in the noise-limited regime).

We note that the dipole optimization problem is mathematically overdetermined; thus a least-squares solution does exist, and in principle nonlinear minimization over the spatial coordinates of the dipole could be used to find it. However, we emphasize that the least-square solution is neither physiologically meaningful (because it invariably overfits the data by using model parameters to account for noise variance) nor robust (because it is easily trapped by odd local minima in the noise regime).

Volume Conductor Model of Brain Tissue

Brain tissue was modeled as a 4-mm-high, 4-mm-diameter cylindrical volume composed of a 2-mm-high cylinder of gray matter sitting on top of a 2-mm-high white matter cylinder. Gray matter and white matter were modeled by passive homogeneous volume conductors with different scalar conductivities ($\sigma_{GM} = 0.45$ S/m and $\sigma_{WM} = 0.15$ S/m). This choice of gray matter conductivity, the geometric mean of the conductivities of the cerebrospinal fluid [$\sigma_{CSF} = 1.37$ S/m (Barber and Brown 1984; Baumann et al. 1997)] and white matter [$\sigma_{WM} = 0.15$ S/m (Barber and Brown 1984)], is physiologically plausible in the sense that it is well within the values measured in various cortices and species (Li et al. 1968; Lopez-Aguado et al. 2001; Ranck 1963; Vigmond et al. 1997). However, ≈ 16 – 33% lower values were used recently in a few modeling studies of pyramidal neurons in neocortex [$\sigma_{GM} = 0.33$ S/m (Moffitt and McIntyre 2005)] or hippocampus [$\sigma_{GM} = 0.30$ – 0.38 S/m (Gold et al. 2007; Gold et al. 2006)]. We note here that, in a homogeneous volume conductor, the particular choice of conductivity affects the inferred dipole moment size but not the accuracy of dipole localization or the estimated recording volume (Mechler and Victor 2011).

As a first (and reasonably good) approximation, gray matter inhomogeneity is neglected here because the estimated effect of laminar variation of volume conductivity in cortex (Lopez-Aguado et al. 2001) on EAP amplitude has been estimated to be modest (Gold et al. 2006).

Tetrode geometry and model. Tetrodes were purchased from the manufacturer, Thomas Recording. Thomas can customize their tetrodes' geometry and contact input impedance; the tetrodes used and the range of parameters reported in this study reflect specifications used in our laboratory for recordings in primate primary visual cortex. General tetrode features (see Fig. 3) include a quartz-insulated shaft shaped as a cylinder and, like a pencil, ground to a cone at the tip in a sharp angle to expose the contacts. Embedded in the quartz coat are four parallel microwires made of platinum-tungsten alloy (PtW), one emerging as the central contact at the center of the tip (the point of the pencil) and three emerging along the tip's sloping portion at equal angles in a concentric arrangement around the central one. The

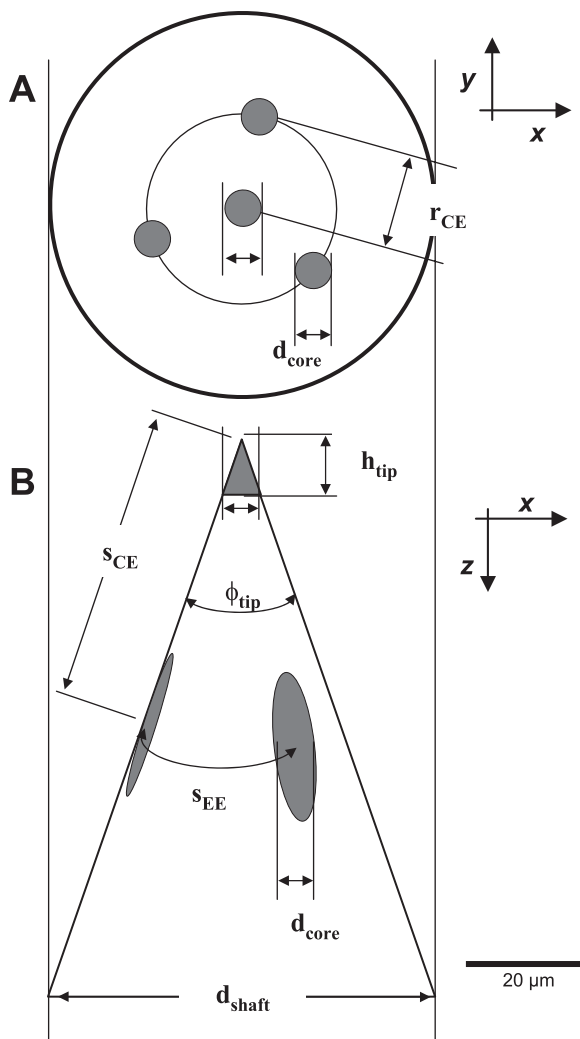


Fig. 3. The geometry parameters used in models of Thomas tetrodes, shown in 2 views: axial (A) and lateral (B). Their definition and their values measured for 4 reconstructed tetrodes are given in Table 1.

geometry of the design guarantees approximate equality of the exposed areas of the elliptically shaped lateral contacts and the conically shaped central contact, and this in turn provides for approximate equality of input impedance on all four tetrode channels. The four contacts also approximate a tetrahedron of equilateral triangles.

The diameters of the wires and the quartz cylinder are constant for the last several hundred microns of their length leading to the conical tip. The angle of the conical tip is adjusted by grinding in the 15–30° range (half-angle measured within a plane on the tetrode's long axis) to achieve target contact impedances. Figure 3 summarizes the geometric parameters of the tetrode tip and shaft that were used to build

Table 1. Parameters used to model tetrode geometry

Tetrode	d_{core} , μm	$\phi_{\text{tip}}/2$, $^{\circ}$	h_{tip} , μm	A_{cont} , μm^2	r_{CE} , μm	s_{CE} , μm	s_{EE} , μm	d_{shaft} , μm	h_{shaft} , μm
03-0591	7	18.5	11	121	17	54	36	63	95
06-3200	8	25	9.5	118	17	40	36	56	60
07-0087	5	26.5	5	44	13.5	30	28	50	50
07-0088	6.5	25	7	78	13.5	32	28	50	54

d_{core} , Diameter of lead wires; $\phi_{\text{tip}}/2$, half-cone angle; h_{tip} , cone height of exposed central contact [= $1/2 d_{\text{core}} \tan(\phi_{\text{tip}}/2)$]; A_{cont} , exposed contact area [= $\pi d_{\text{core}}^2 / \sin(\phi_{\text{tip}}/2)$ for both center and eccentric]; r_{CE} , lateral axis-to-axis separation of the center and the eccentric core wires; s_{CE} , center-to-center separation of center and eccentric contacts [= $r_{\text{CE}} / \sin(\phi_{\text{tip}}/2)$]; s_{EE} , center-to-center arc separation of two eccentric contacts (= $2\pi r_{\text{CE}}/3$); d_{shaft} , shaft diameter; h_{shaft} , cone height of entire tip below shaft cylinder.

the model tetrodes. The values (Table 1) were measured from high-resolution scanning electron microscopic (SEM) images (not shown) taken of four of the seven tetrodes used in this study after the completion of the stepping experiments.

In our tetrodes, contact impedance at 1 kHz was 1.4 ± 0.25 MOhm, individually tested and certified by Thomas Recording. The specific conductivity of the model conductor was modeled by the mean ($\sigma_{\text{P,W}} = 1.5 \times 10^7$ S/m) of the two alloy components, and that of the quartz shield, as the ideal insulator ($\sigma_{\text{vacuum}} = 0$ S/m).

In the finite element model, the tetrode was introduced into the cortex along the axis of the brain cylinder, with its tip halfway down the gray matter. The outer boundary of the brain cylinder was grounded, except at the top, where it was insulated. To calculate a lead field, the selected tetrode lead was clamped at a unit current, and all other tetrode boundaries were insulated.

The “Exact Probe” and “Approximated Probe” Sets

Since it is often not possible to measure tetrode geometry directly, we were interested in determining the importance of the precise geometry for the model fit. In our experiments, three of the seven tetrodes could not be scanned, and we had to approximate their geometry in the model. This distinction defined two subsets of our data, one recorded from tetrodes whose measured geometry was determined from SEM images (“exact-probe” set; $n = 43$) and the other (“approximated-probe” set; $n = 18$) recorded from tetrodes whose geometry was modeled by the median among the imaged tetrodes (the median tetrode is listed second in Table 1 and used in Fig. 2). To determine the importance of knowing the precise geometry, we maintain this distinction between these subsets in the analysis below.

The dipole fit and its error. The quality of a typical dipole fit in an exact probe data set is illustrated in Fig. 2B. The EAP amplitudes predicted by the optimal dipole (lines) correspond closely with the measurements (symbols) on all four tetrode channels; they account for 95% of the power in this data set. The term “power” is used here in the standard way, the variance in the data around zero. More precisely, for a measure of fitting error, the mean squared error (MSE) was divided by the average of the squared voltages in the data (the data power) to calculate the fractional MSE (fMSE):

$$\text{fMSE} = \frac{1}{4N_{\text{step}}} \sum_{i=1}^{N_{\text{step}}} \sum_{k=1}^4 (V_{i,k} - \tilde{V}_{i,k})^2 \bigg/ \frac{1}{4N_{\text{step}}} \sum_{i=1}^{N_{\text{step}}} \sum_{k=1}^4 V_{i,k}^2,$$

where $V_{i,k}$ and $\tilde{V}_{i,k}$ are, respectively, the EAP amplitudes measured and predicted on the k th tetrode channel at the i th tetrode location (“step”).

Using the spatial EAP sample constructed for peak EAP time (as in Fig. 2), we similarly solved the optimal equivalent dipole source for each of the 61 neurons in our sample. On average, the dipole model captured ~96% of the power in the spatial EAP data, leaving a fMSE of 4%. On average, only 1% of the fitting error can be attributed to uncertainty in the EAPs; the 95% confidence half interval ($2 \mu\text{V}$) divided by the mean EAP ($98 \mu\text{V}$) and then squared represents $(2/98)^2$

$\approx 0.04\%$ fMSE. Thus most of the error was systematic, i.e., a model error. In the cell of Fig. 2*B*, for example, the rate of potential variation with probe position appears faster than what a dipole predicts, probably indicating a quadrupole contribution.

The various potential sources of localization error are addressed in detail in the accompanying paper (Mechler and Victor 2011). One form of model error relates to the probe geometry. The fitting error in the exact probe set (fMSE = 3%, range 1–11%; $n = 43$) was significantly lower than in the approximated probe set (fMSE = 6%, range 1–30%; $n = 18$). Thus, although tetrode models built with a lack of knowledge of the exact geometry lead to larger errors in dipole characterization, the fitting error is still acceptably small in most cells.

Another potential localization error is a bias that the choice of source model class introduces. We show that, for recordings in most cortical areas, the dipole could slightly overestimate (by ≈ 10 –15%) typical cell-probe distances. However, the monopole severely underestimates distances (by at least $\approx 50\%$). Because experimental data on the true position of the isolated neurons is undisputedly difficult to get, we addressed the question indirectly via model simulations and reanalysis of data from other laboratories. We give a brief summary here.

In the first set of simulations [2nd supplemental material of the companion paper (Mechler and Victor 2011)], we aimed to determine how well we can recover the direction and distance of various kinds of known model sources (e.g., monopole, dipole, quadrupole, or distributed like in a real cell) by localization that assumes that the source is a monopole or a dipole. An interesting and perhaps surprising aspect of one of these analyses is that the amount of data power explained by the source model is not an indicator of localization accuracy. As these simulations, as well as mathematical analysis, show, localization accuracy strongly depends on how well the assumed source model matches the characteristics of the actual source. In particular, a monopole underestimates a dipole's distance by one-half, and when the roles are reversed a dipole overestimates a monopole's distance by a 100%, even though the fitting errors are very small and comparable in both scenarios. In general, the monopole has a larger localization error for sources that have significantly higher moments, like the distributed sources of real neurons. A key insight related to this latter point is presented in the 1st supplemental material of the companion paper (Mechler and Victor 2011). There we show, by reanalyzing both real data and realistic neuron models from other laboratories, that the field around real neurons, beyond a minimum distance (e.g., $>r_0 \approx 30 \mu\text{m}$), has a radial decay that resembles the dipole. We note that r_0 and a dipole-like regime that holds for distances beyond r_0 has been predicted by the analysis of passive cable models, using realistic geometry of cortical pyramidal and stellate neurons (Pettersen and Einevoll 2008). That study and the results of the first set of our simulations together predict that, for fields like those around neurons at distances $>r_0$, the monopole would underestimate the cell location by as much as 50%. In contrast, the dipole model under the same conditions does a very good job. We show this in a second set of simulations in which the source field has a radial decay that resembles the one around real neurons; for cell-probe distances $>r_0$, we find that the dipole model makes a modest ($\approx 15\%$) overestimation of source distance.

Sample Pooling

After completing the dipole localization analysis for each neuron, we retrospectively checked for the validity of pooling across subsets that differed in cortical areas (V1 vs. V4), species (cat vs. monkey), probe size (contact separation varied by $\leq 50\%$), or whether probe size was known or not known. Only the known difference in probe size was statistically significant. Specifically, the size and distance of the optimal dipole in the different subsets did not differ by $>25\%$ across areas and species. Mean cell-probe distance was significantly larger ($P < 0.03$, 2-sample *t*-test) in the subset probed with the largest

tetrode (109 μm) than the smallest tetrode (92 μm). The tetrodes involved are those listed in the first and third rows of Table 1.

Finally, subset variances were not significantly different ($P > 0.03$, Levene's test) whether defined by tetrode or by tissue.

RESULTS

We used dipole localization to quantify three major aspects of the spatial sensitivity of tetrodes: 1) their estimated recording volume, 2) the isolated fraction of neurons within that volume, and 3) the sampling anisotropy and localization precision of the tetrodes in isolating these neurons. We also address 4) the distribution of the equivalent dipole size (strength of current source) and the orientation of its moment vector in cortical neurons. Finally, to highlight the utility of dipole localization, 5) we reconstruct the position of recorded neurons along the electrode track.

Neuron Sample

The sample population consisted of 61 single neurons from visual cortex. The cells were isolated in 11 stepping experiments made with seven tetrodes in one cat and two monkeys (the animals were used in conjunction with other experiments reported elsewhere). Thus, on average, a tetrode isolated six single neurons along a 90- μm -long track (the most was 13). The sole cat experiment yielded 10 neurons on a single track in area 17. In the monkey experiments, multiple tetrodes were simultaneously placed and used at multiple cortical depths; some were in V1 (a total of 18 single cells), and others were in V4 (a total of 33 single cells).

Recording Volume

The six examples shown in Fig. 2, *B–G*, illustrate the range of the quality of the dipole fit in our sample. In each case, except for the cell in Fig. 2*C*, the optimal dipole accounted for $>95\%$ of the power in the spatial EAP data (sampled at peak EAP time, as indicated by the vertical line in Fig. 2*A*). This was typical of our sample; across the 61 neurons in our sample, the dipole model captured $\sim 96\%$ of the power in the spatial EAP data.

We use the dipole fits to characterize the volume of brain in which a tetrode can isolate the action potentials of single neurons. To do this, we analyze the distribution of cell-probe separations. We define this as the distance between the spatial location of the optimal dipole fitted to each neuron and the location of the recording tip in the step where the EAP of the neuron was first discriminated as a single unit (the results were not significantly different in an alternative analysis that used the step position nearest to the cell). We first consider the population distribution of cell-probe distances and then refine the analysis to take into account the direction of the neuron from the recording tip.

There are two ways to characterize the dependence on distance. From the point of view of the tetrode, it is useful to know the distribution of distances to neurons that the tetrode can isolate. This leads to an estimate of the recording radius of the probe. From the point of view of a specific neuron, it is useful to know how the probability of isolation depends on distance from the probe. This leads to an estimate of the recording radius of a neuron. The two are related but need not be equal because they reflect different probabilities.

The tetrode's point of view is taken in Fig. 4A, *top*. Half of the isolated neurons are located within a radius of $R_{50} = 97 \mu\text{m}$; 95% are within a radius of $R_{95} = 132 \mu\text{m}$. This distribution indicates the probability that a tetrode records a neuron at a radius r . The recording radii analyzed separately for the exact probe subset ($R_{50} = 94 \mu\text{m}$) and approximated probe subset ($R_{50} = 106 \mu\text{m}$) were not significantly different ($P > 0.4$, Wilcoxon rank sum test) (note that these measurements are medians).

To change to the neuron's point of view, we need to determine the relative probability with which a neuron at a given location is isolated; this is the local isolated fraction (a volume density function). This quantity varies with spatial position around the probe and measures locally (i.e., within an infinitesimal volume around a given spatial location in 3-dimensional space) the expected number of isolated neurons as a fraction of the number of locally present neurons. Assuming spherical symmetry of probe sensitivity, this density function depends only on the radial distance r from the probe, so it is proportional to the probability that a tetrode records a neuron at a radius r (identical to that of Fig. 4A), but it is divided by the number of cells available within the volume of a probe-centered thin spherical shell of radius r . Assuming uniform cell distribution, the latter is the product of the shell volume and the average numerical neuron density obtained from the literature [we used $n \approx 0.12 \times 10^6 \text{ mm}^{-3}$, typical estimates for

macaque V1 (Cragg 1967; O'Kusky and Colonnier 1982)]. To get the normalization right, the fraction must also be multiplied with the average number of simultaneously isolated neurons, N_{isol} , that is experimentally determined for a probe (we used $N_{isol} = 3.6$, as determined in the section dedicated to the "isolated fraction" below; note that the overall isolated fraction we report there is the volume average of this local isolated fraction).

Results of this calculation are shown in Fig. 4A, *bottom*. The histogram (Fig. 4A, *bottom*, open bars), obtained by binning the data in $20\text{-}\mu\text{m}$ -thick spherical shells, shows a rough estimate; the smooth curve is the kernel density estimate free of binning artifacts and incorporates in a principled way the measured uncertainty about the location of each cell (for details, see legend to Fig. 4). The shaded domain indicates the bootstrap estimate of the 95% confidence limits around the curve. The local isolated fraction is low (<0.01) everywhere, but it varies with radial distance from the probe, and its behavior can be roughly divided into two domains at an inflexion point near $90 \mu\text{m}$. For radial distances $>90 \mu\text{m}$, the fraction declines monotonically and fast. For radial distances $<90 \mu\text{m}$, the fraction hovers in the $0.002\text{--}0.005$ range, with a small local peak near $70 \mu\text{m}$ and a small dip near $50 \mu\text{m}$. The large oscillation in the local isolated fraction seen for distances $<50 \mu\text{m}$ is unreliable (confidence limits are wide and include zero) because this part of the distribution represents only three cells. The radial

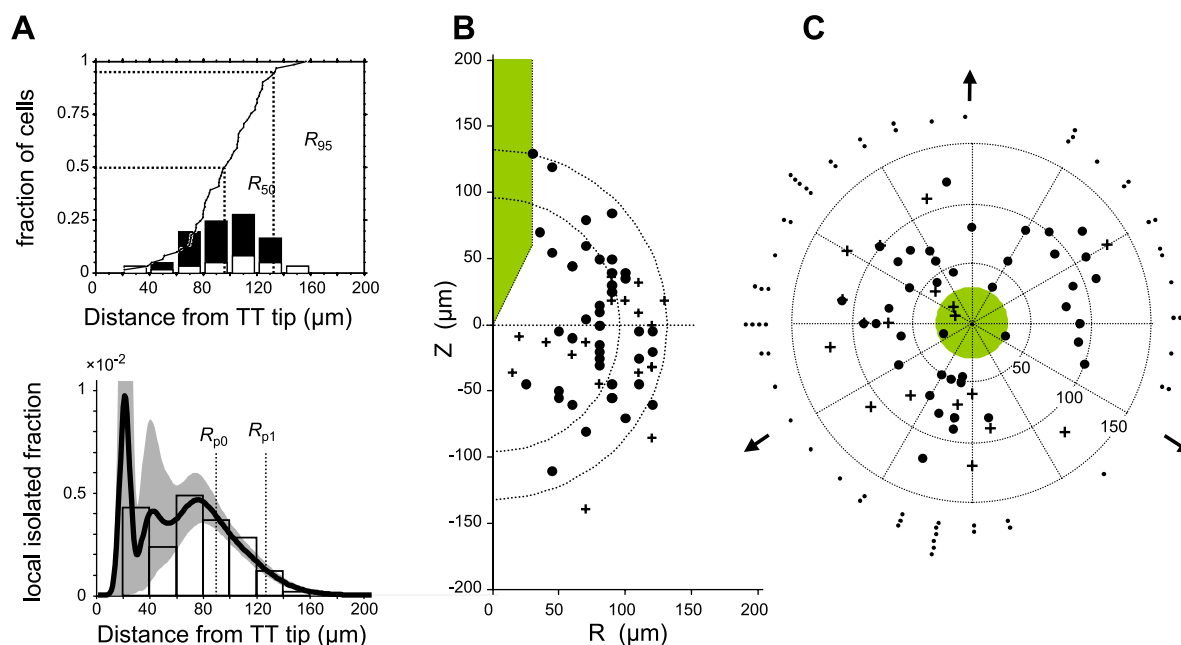


Fig. 4. Analysis of the 3-dimensional distribution of the cell position relative to the tetrode as determined by the optimal dipole loci. *A*: characterization of the recording volume of the Thomas tetrode in visual cortex. *Top*: characterization via percentiles of distances to isolated neurons. Closed bars represent the exact probe subset (median $94 \mu\text{m}$; $n = 43$); open bars represent the approximated probe subset (median $106 \mu\text{m}$; $n = 18$). *Bottom*: the radial variation of the local isolated fraction, i.e., the volume density of the number of isolated single cells as a fraction of the locally available neurons. For the kernel estimate (smooth curve), cell location probability was modeled with 3-dimensional Gaussians with adaptive bandwidth; i.e., the standard deviation of the Gaussian was $1/3$ of the scatter radius measured for each cell. This guaranteed that $>96\%$ of the probability mass of the kernel was contained within the scatter radius, consistent with its definition; see RESULTS for scatter radius below. Shaded area indicates the bootstrap estimate of the 95% confidence limits. *B*: the distribution of dipole loci projected on the plane of vertical (Z) vs. radial (R) axis by sweeping the x - y plane around the tetrode axis ($R = 0$). The origin is at the tetrode tip, and the space occupied by the tetrode is shaded. The inner and outer semicircles enclose the volumes corresponding to R_{50} and R_{95} , respectively. ● Exact probe subset ($n = 43$); + approximated probe subset ($n = 18$). The recovered R - Z coordinates (in μm) of the 6 examples in Fig. 2, given in their order of presentation, are (60, -10), (80, -30), (90, 18), (110, -25), (90, 40), and (100, -70). *C*: the x - y distribution of the optimal dipoles (z -coordinates collapsed); symbols show same subsets as in *B*. The arrows indicate the azimuth direction of the eccentric leads. The coordinate rings with 100- and 150- μm radii approximate R_{50} and R_{95} , respectively. The dots stacked outside the 150- μm ring represent the binned azimuth distribution.

distance, $R_{p0} = 90$, where the isolated fraction has its inflexion point (left vertical line), corresponds closely to R_{50} . The radial distance, $R_{p1} = 125 \mu\text{m}$, where the isolated fraction drops by a factor of $1/e$ (right vertical line), corresponds closely to R_{95} .

These raw estimates of recording radius may be overestimates by 10–15% due to biases related to the dipole model [see DISCUSSION and also the companion paper (Mechler and Victor 2011)].

We also note that the lead field radii of the individual contacts provide a first approximation for the recording radius of the tetrode as a whole. The extent of the lead field can be determined in terms of an equivalent contact potential defined with a standard dipole source. Specifically, we define the “lead field radius” as the distance from the lead at which a neuron with a dipole moment of typical strength (and optimal alignment with the lead field vector at all positions) produces a signal that reaches a criterion voltage that corresponds to isolation threshold (for further details, see Mechler and Victor 2011). Using the average dipole moment in visual cortex of $5 \text{ pA} \times \text{m}$ (see below) and a criterion potential set near isolation threshold ($\approx 50 \mu\text{V}$), the lead fields of both central and eccentric contacts were found to be $r_{50\mu\text{V}} \approx 135 \pm 3 \mu\text{m}$. The R_{95} tetrode radius is larger than those field radii but smaller than the radius of the union of the fields.

Next, we examined how isolation depended on the direction from the probe tip to the neuron. We reference neuron location to the position of the tetrode where each neuron’s EAP was first isolated along the track, using cylindrical coordinates centered at the tetrode tip: the distance along the track (Z), the radial distance from the track (R), and the azimuth (θ). Figure 4B shows the R vs. Z joint coordinate distribution along with semicircles corresponding to r_{50} and r_{95} . Note that no neurons were located in the space occupied by the tetrode (shaded area). This was not built in to the fitting procedure and serves as a check on its accuracy. The dependence on elevation was consistent with random sampling. The apparent slight bias toward cell positions located below the tetrode tip (negative z -coordinates) in the approximated probe set (Fig. 4B, + symbols) was not significant ($n = 18$, 1-sided t -test, $P > 0.08$); no such bias was present in the exact probe subset ($n = 43$, 1-sided t -test, $P > 0.5$; Fig. 4B, ●). Another apparent bias, one toward the near-equatorial elevations, is accounted for by a volume effect; 79% of neurons are located within the middle 90° of elevation centered on the equatorial plane; this is not significantly different from the 71% expected from a homogeneous distribution ($P > 0.1$; $n = 61$, bootstrap test).

On the other hand, the dependence on azimuth was not random (Fig. 4C). In the joint distribution of the radial and azimuth coordinates (symbols as in Fig. 4B), there was a preponderance of neurons that were located in azimuth directions in between rather than toward eccentric contacts (the latter face in the direction of the 3 arrows 120° apart). This bias is statistically significant for both the exact probe subset (circular mean test applied to $3 \times$ azimuth, $P < 0.02$, $n = 43$) and the approximated probe subset ($P < 0.05$, $n = 18$). Although we cannot rule out fitting bias, we think the threefold symmetry of the bias in azimuth sensitivity is likely due to synergy between the pairs of eccentric leads; cell isolation is more likely if the cell can be recorded from at least two eccentric leads, and this is most likely to happen in planes that

are about equally distant from two eccentric leads of the tetrode. In those directions, the field strength of two eccentric leads will be comparable, and more importantly, the lead field vectors will be more likely to be similarly aligned [in an approximately radial direction; see azimuth profile of the distortions in the eccentric lead fields in the companion paper (Mechler and Victor 2011)]. The two factors, especially the second one (which is much less dependent on cell distance), are necessary for two eccentric leads to register EAP with sufficient S/N from the same dipole source. Indeed, as expected of good tetrode-like recordings, the extracellular records of most isolated cells had a good S/N (> 2 ; see METHODS) on at least three of the four tetrode leads, always including the central lead.

Precision of Dipole Localization

The above dipole characterization assumes that the neural spike generator is a spatially fixed, temporally modulated current source. We exploit the temporal redundancy in this assumption to assess the precision of dipole localization. Specifically, we fitted the point dipole model independently to samples of the EAP waveforms obtained at five instances, spanning both the negative and positive deflections in the spike waveform. As a measure of precision, we determined the “scatter radius,” the radius of the smallest sphere that contained all five location estimates. Note that this estimate is a conservative one, since it is possible that part of the scatter reflects genuine source dynamics; over the course of an action potential, the dominant currents could change positions, e.g., as the somatic depolarization propagates to the dendrites.

The distribution of the scatter radius (Fig. 5A) indicates that precision is $60 \mu\text{m}$ or better for 47 of 61 (77%) of the cells. The mean for the entire sample was $\approx 51 \mu\text{m}$ ($n = 61$) and not significantly different for the exact probe and the approximate probe subsets (47 vs. $60 \mu\text{m}$; $P > 0.15$, t -test). Intuitively, one would expect that precision is better for neurons that are close to the probe. This is confirmed in Fig. 5C, which plots the scatter radius (from Fig. 5A) against the estimated distance (Fig. 5B, replotted from Fig. 4A). Indeed, these two quantities are significantly correlated ($r^2 = 0.42$, $P < 0.001$); the scatter radius is approximately one-half of the estimated distance. [Note that the scatter radius cannot be explained by the localization error attributed to the discrete spatial sampling of the finite element model (Fig. 5C, bottom dashed line).] Thus the typical neuron can be localized within a spherical volume whose diameter is approximately the same as its distance from the probe. In other words, the spherical volume of uncertainty about a cell’s location is approximately an order of magnitude smaller than the spherical recording volume. The directional uncertainty is even smaller. Viewed from the tetrode tip, the sphere of uncertainty around the location estimate occupies approximately one-fifteenth of the 4π solid angle represented by the entire recording volume. This is calculated as follows. The angle of the viewing cone, whose vertex is at the tetrode tip, is defined by the distance, R , of the cell from the tetrode tip and the radius, r , of the uncertainty about the location of the cell. The vertex angle of the cone, 2θ , is determined by the radii as $\sin\theta = r/R$, and the solid angle of the cone, Ω , is in turn determined by the vertex angle as $\Omega = 2\pi(1 - \cos\theta)$. Substituting $\sin\theta$, using the identity $\sin^2\theta + \cos^2\theta = 1$ and expressing Ω

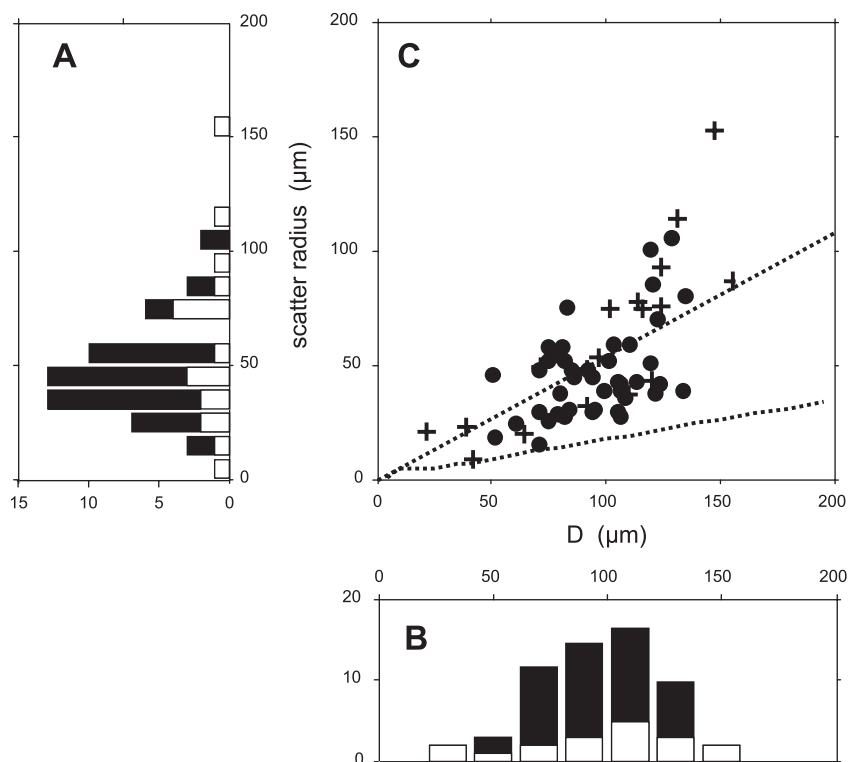


Fig. 5. Precision of spatial localization using a dipole model. *A*: distribution of the scatter radius, a measurement of localization error. It is defined as the radius of the cortical volume enclosing the loci of optimal dipoles independently fitted to a neuron at different times into the action potential. Overall mean, 51 μm ($n = 61$). The exact probe subset (closed bars; mean 47 μm , $n = 43$) and the approximated probe subset (open bars; mean 60 μm , $n = 18$) were not significantly different ($P > 0.16$, t -test). *B*: distribution of the 3-dimensional distance of the tetrode tip from the optimal dipole locus at peak action potential time (reproduced from Fig. 4*A*, top). Means (not medians): overall, 96 μm ; exact probe subset, 95 μm (closed bars); approximated probe subset, 98 μm (open bars). *C*: joint distribution of the above 2 parameters. Circles depict the same cells as those represented by closed bars, and plus symbols depict the same cells as those represented by open bars in *A* and *B*. Linear regression (top dashed line) identifies a significant correlation with a positive slope (0.54, $P < 0.001$). Similar results hold separately for circles (0.49, $P < 0.001$) and the plus symbols (0.64, $P < 0.01$). The bottom dashed line is the localization uncertainty expected from the discrete spatial sampling of the finite element model.

as fractions of the full solid angle, we get $\Omega/4\pi = (1/2)(1 - (1 - (r/R)^2)/2)$.

For the average radii in our data, $r/R \approx 1/2$ and $\Omega/4\pi \approx 1/15$.

The scatter radius was larger in the approximated probe subset (Fig. 5*C*, open bars or + symbols) than in the exact probe subset (Fig. 5, closed bars or circles), but the proportionality between them remained the same.

The Isolated Fraction of Cortical Neurons

Our analysis of the recording volume allows us to estimate f_{isol} , the isolated fraction associated with tetrode recordings in visual cortex. This fraction, $f_{isol} = N_{isol}/N_{tot}$ is the ratio of the expected number of isolated neurons, N_{isol} , over the expected total number of neurons, N_{tot} , within the spherical recording volume, V_{rec} , of a stationary tetrode. We directly determine N_{isol} from tetrode stepping experiments, calculate V_{rec} from the recording radius inferred from source localization, and derive N_{tot} from published estimates of the numerical neuron density, n , in the probed brain area as $N_{tot} = nV_{rec}$.

The spherical recording volume of a stationary tetrode, of recording radius, R , is $V_{rec} = (4\pi/3)R^3$. The tetrode passing through a track segment of length, h , probes a brain volume, V_{track} , that is larger than V_{rec} by the $\pi R^2 h$ volume of an h -long cylinder of the same radius, i.e., $V_{track} = V_{rec} + \pi R^2 h$ or $V_{rec}/V_{track} = 1/(1 + 3h/(4R))$. The stepping experiments provide for a direct estimate of N_{track} , the average yield of isolated neurons in a single experiment; of this, N_{isol} is the same fraction as V_{rec} is of the total volume probed along the track: $N_{isol}/N_{track} = V_{rec}/V_{track} = 1/(1 + 3h/(4R))$.

Our experiments yielded two to 13 neurons per track, 61 in total on 11 tracks, making $N_{track} \approx 5.5 \pm 4.0$ (mean with 95% confidence interval). The high variability of yield is attributable to factors other than track length ($h \approx 90 \pm 10 \mu\text{m}$).

Taking $R = R_{95} \approx 132 \mu\text{m}$, the recording radius within which 95% of isolated neurons were located (Fig. 4), leads to $N_{isol} \approx 3.6 \pm 2.6$ in $V_{rec,95} \approx 9.6 \times 10^{-3} \text{mm}^3$. Assuming $n \approx 0.12 \times 10^6 \text{mm}^{-3}$ (Cragg 1967; O'Kusky and Colonnier 1982), a consensus estimate of neuronal density in monkey visual cortex, the expected total number of neurons in $V_{rec,95}$ was $N_{tot} \approx 1,150$, making the isolated fraction $f_{isol} = N_{isol}/N_{tot} \approx 0.0031 \pm 0.0023$, or slightly less than 1 in 300.

The alternative definition of the recording radius, $R = R_{50} \approx 96 \mu\text{m}$, leads to a slightly larger isolated fraction. This choice, which corresponds to a 50% yield ($N_{track}/2$), leads to $N_{isol,50} \approx 1.6 \pm 1.2$ and $N_{tot,50} \approx 440$ in $V_{rec,50} \approx 3.7 \times 10^{-3} \text{mm}^3$ and yields $f_{isol,50} = N_{isol,50}/N_{tot,50} \approx 0.0036 \pm 0.0027$ or slightly more than 1 in 300. This calculation highlights the nonlinear dependence of the isolated fraction on the distance from the probe; it remains near its maximum at close ranges (Fig. 4*A*, bottom), and it gradually declines for $r > R_{50}$ distances.

Note that the estimate of f_{isol} can range widely and is also subject to some uncertainty. If the same calculation used the more recent estimate of the numerical density in macaque V1 (Collins et al. 2010), which is 30–50% greater than the older consensus we cited above, f_{isol} could be as low as 0.002 (similarly, the cell density estimated in V4 in the same study would make the isolated fraction 0.004 in V4). Importantly, the Collins et al. study also documented strong cell density variations with cortical representation of visual eccentricity, implying that the isolated fractions could be significantly different for the same tetrode used in different areas of the visual cortex in the same animal. The upper bound on the fraction that these tetrodes can isolate in visual cortex is likely near $\approx 2\%$. This is the f_{isol} value in our sole cat experiment, benefiting from a higher than average yield ($N_{track} = 10$) and a lower numerical density [$n \approx 0.05 \times 10^6 \text{mm}^{-3}$ (Beaulieu and Colonnier 1987)] than in monkey.

These raw estimates of isolated fraction are underestimates by $\sim 8\%$, due to ignoring the volume occupied by tetrode itself, and may be by another 20–30%, which is due to a possible 10–15% overestimation of source distances by the dipole model [see DISCUSSION and also the companion paper (Mechler and Victor 2011)]. (The implied overestimation of V_{track} was derived from its dependence on the recording radius as above).

The Equivalent Dipole Moments

Dipole characterization yields, in addition to the location, an estimate of the dipole moment vector that characterizes apparent magnitude and orientation of the equivalent current source of the isolated neuron.

Figure 6A shows, on a log scale, the distribution of the dipole moment magnitude, $\|\mathbf{p}\|$, in our pooled sample. It has a single peak, positioned approximately at the median ($4.48 \text{ pA} \times \text{m}$), and the bulk ($\approx 90\%$) of the sample falls within a log unit interval centered on the peak (1.6 to $16 \text{ pA} \times \text{m}$). The medians were indistinguishable in cat vs. monkey cortex ($P > 0.80$, Wilcoxon rank-sum test) and in V1 vs. V4 ($P > 0.09$, Wilcoxon rank-sum test). The continuous shape and single mode indicate no distinct categories of cortical neurons that could be identified by the equivalent current source size. We could not assess laminar dependence, because histological

track reconstruction was available in only a minority of these experiments.

Differences in tetrode geometry (as expected) did not significantly influence the inferred dipole size. However, knowing the probe geometry exactly did make a difference (Fig. 6B): the dipole size, $\|\mathbf{p}\|$, was larger by a ≈ 1.26 factor in the approximated probe subset than in the exact probe subset ($P < 0.05$, Wilcoxon rank-sum test). Given that the measured EAP amplitudes, V , were comparable, the increase in $\|\mathbf{p}\|$ is almost entirely explained by the ≈ 1.13 increase in the apparent source-probe distance, (D ; Fig. 5), together with the $V \approx \mathbf{p}d^{-2}$ potential falloff of dipole fields.

We also analyzed the orientation of the equivalent dipole, and this proves important in understanding its origin. There was a strong tendency for the equivalent dipole to point toward the probe (Fig. 6B). In this summary figure, each unit vector indicates the direction of one cell's dipole moment vector, referenced to the direction from the probe to the cell. To bring the cells into this common reference frame, each cell's dipole direction vector was rotated (first in the azimuth plane, next in the orthogonal plane) by an amount that was required to realign the same cell's probe-to-cell direction with the red bar in this plot. Thus, with respect to the original coordinates of the dipole direction and the probe-to-cell direction, the angular coordinates shown in Fig. 6B are the relative azimuth (varying in the

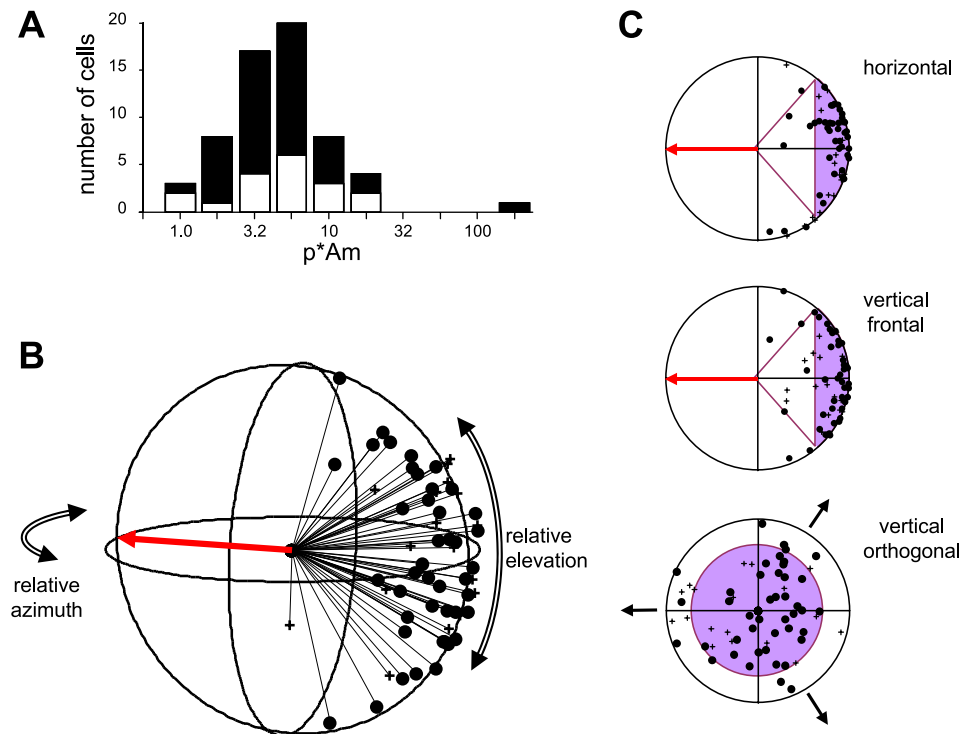


Fig. 6. The equivalent dipole determined for a sample of $n = 61$ neurons in visual cortex. *A*: the distribution of the log magnitude of the equivalent dipole moment ($\text{pA} \times \text{m}$). The median dipole moment is $4.5 \text{ pA} \times \text{m}$ (coinciding with the mode of distribution on log scale). The closed-bar portion of the histogram shows the exact probe subset (median $4.4 \text{ pA} \times \text{m}$), and the open-bar portion shows the approximated probe subset (median $5.6 \text{ pA} \times \text{m}$). *B*: the relationship between the dipole moment and the direction from the probe to cell. For each cell, the measured direction of the optimal dipole moment vector is plotted as a unit vector, following transformation into a frame in which the probe-to-cell direction is aligned to the red arrow. Specifically, the azimuth of each plotted vector (around the horizontal circle) is the azimuth of the cell's dipole relative to the azimuth of the cell position, and the elevation (above or below the horizontal plane) is the elevation of the cell's dipole relative to the elevation of the cell's position. The symbols, indicating the end points of the unit vectors, depict the same 2 subsets as before. *C*: 2-dimensional projections of the data in *B*, with the shaded area indicating a conical domain of 50° half-angle. The conical domain is predicted by cell morphology (see text). Projections are on the azimuth plane (*top*), the frontal vertical plane (*middle*), and the orthogonal vertical plane (*bottom*) (red bar is behind the plane). In 75% of the cells, the optimal dipole direction was within the conical domain, i.e., within 50° of alignment to the cell-to-probe axis. Subsets and corresponding symbols are as defined in METHODS and shown as described in Figs. 4 and 5.

horizontal equatorial plane) and the relative elevation (varying in the vertical plane; it is zero in the horizontal plane).

Figure 6C shows the planar projections of the data in Fig. 6B. Approximately 75% of the dipoles are within 50° of the cell-probe direction (shaded domain), and they appear to be randomly distributed. The remaining 25% of the sample differs from the majority by exhibiting excessive (i.e., $>50^\circ$) departure from the cell-to-probe direction in azimuth (Fig. 6C, top) and/or elevation (Fig. 6C, middle). Figure 6C, bottom, reveals that the departures in dipole azimuth and elevation (relative to the cell direction) are correlated with each other. Moreover, these outliers exhibit a threefold symmetry (indicated by 3 black arrows 120° apart) of the directional variation of tetrahedral tetrode sensitivity. A similar threefold pattern was seen in the x - y coordinates of the recovered cell locations (Fig. 4C).

The expected alignment of the dipole vector with the cell-to-probe direction (opposite the red bar in Fig. 6) can be estimated by the angle of the vector mean of the rotated unit dipole vectors; its deviation from the direction of the cell-probe axis was $<4^\circ$ and not significant ($P > 0.50$; jackknife), and the sample median of the deviation calculated for each cell, a measurement of scatter around the cell-probe axis, was 33° .

Finally, we provide the statistics on the angular coordinates of the cell location (defined by the probe-to-cell vector) and the dipole moment vector in unrotated coordinates. (Note that, because of a sign convention of probe-centered coordinates, a dipole moment vector that is aligned with the cell-to-probe vector will have the opposite elevation and an azimuth that differs by π rad.) Thus, consistent with the above alignment of these vectors, moment elevation was significantly anti-correlated with location elevation (circular correlation coefficient less than -0.8 , $P < 0.01$), and their sum was not significantly different from 0 rad (circular mean test, $P > 0.3$). Moment azimuth was significantly and positively correlated with location azimuth (circular correlation coefficient >0.7 , $P < 0.001$), except in the approximated set ($P > 0.06$); they were maximally out of phase, as indicated by their difference not being significantly different from π rad (circular mean test, $P > 0.4$).

This analysis was on EAP samples taken near the negative voltage peak; for samples taken at a time after the voltage polarity flipped, the results are similar, except then the moment and location vectors tend to be aligned rather than opposed (not shown).

In summary, Fig. 6 shows that the direction in which the probe encounters a neuron determines the orientation of the equivalent dipole moment of the cell. This is at first sight quite puzzling, since one might expect that the dipole direction is fixed (by the geometry of the cell), and the direction of encounter is random. In the DISCUSSION, we introduce the notion of the local lobe to show how this unexpected observation can arise, how it sheds light on the nature of the “equivalent dipole,” and how it is related to the nature of the dendritic arbor. Accordingly, the confinement of the data in Fig. 6 within a conical domain can be taken as a vivid illustration of the local lobe; the unit vectors trace the solid angle footprint of the average local lobe of dendrites on the typical visual cortical neuron that our tetrode isolates.

Track Reconstruction and Spatial Configuration of Local Ensembles

The above dipole localization technique makes it possible to reconstruct the spatial configuration of a simultaneously recorded local ensemble as a tetrode is stepped along a track.

Figure 7 provides a proof of principle, illustrating the reconstruction of the spatial configuration of a local ensemble of eight neurons along a $90\text{-}\mu\text{m}$ -long track. At each of the 10 recording positions in this experiment (represented by the dots along the track line below the tetrode pencil in Fig. 7), it was possible to isolate signals from at least four neurons. The equivalent point dipole source of each neuron was estimated at five successive moments in action potential time (as described for the scatter radius above). Note that for each cell the five location estimates scatter within a volume that is easily distinguished from those associated with other neurons; the localization precision is good enough, and the isolated fraction is low enough to discriminate between distinct sources (neurons) within the simultaneously recorded ensemble. This reconstruction also demonstrates that one can estimate the relative distances of pairs of neurons with a precision that is much greater than the limits of the recording radius. This inference follows because the accuracy of each cell’s location is determined by

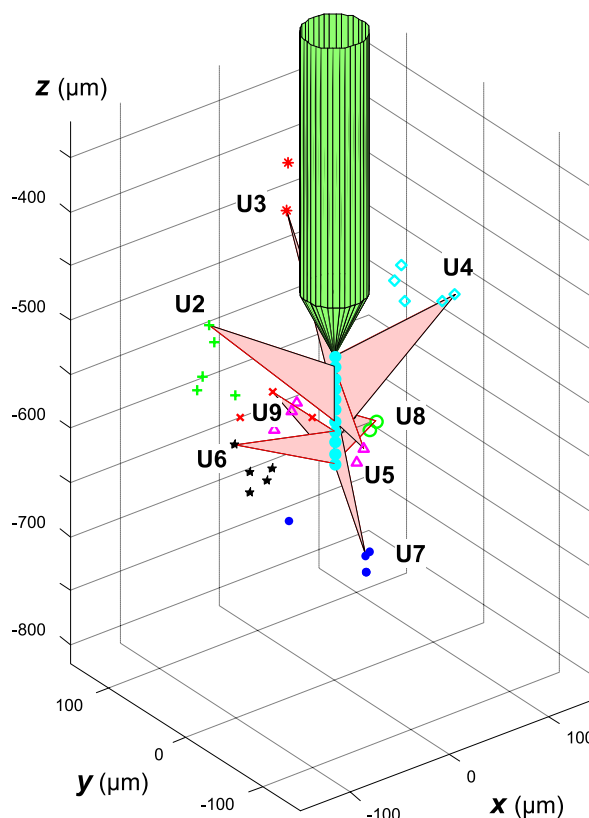


Fig. 7. The spatial configuration of a local ensemble of single units in visual cortex identified and localized from a single tetrode-stepping experiment. The steps spanned a $90\text{-}\mu\text{m}$ segment of the track (line in cyan). The green “pencil” represents the tetrode in its position at the 1st step. Different symbols (and colors) represent each of the 8 identified neurons (U2–U9), and 5 of the same symbol represent the same neuron as localized by the optimal dipole fitted at 5 different moments in action potential time. Triangles point to the locus of the dipoles fitted at peak action potential time, and the base of a triangle indicates the linear span along the track in which the corresponding neuron could be isolated.

the scatter radius, which is much smaller than the recording radius (Fig. 5). Thus, in a typical recording that supports dipole localization (e.g., the one shown in Fig. 7 made with a stepped tetrode), the individual locations of two neurons can be readily resolved, even though both are within the recording radius of the probe. In contrast, for a single electrode or an unstepped tetrode, the neurons' positions cannot be resolved within the recording radius, nor can be the distance between any pair of such neurons (the best estimate of the distance is comparable with the recording radius and the same for all pairs). The greater precision of the dipole-localized neurons' positions leads to a correspondingly greater precision of the distances between the neurons.

Spatial reconstructions similar to the one shown were obtained for a total of 11 local ensembles, each consisting of five to six neurons on average, recorded in separate stepping experiments, all spanning comparable track lengths. In all cases, single units were as discernable as in this example.

DISCUSSION

Summary

We have investigated the spatial sensitivity of tetrodes for single-unit recording in the brain. The tetrodes studied have a rigorously specified geometry (tetrahedral contact configuration; Thomas Recording), and the brain areas we focused on (visual cortex of monkey and cat) are well characterized and often studied with such probes. The basic strategy was to advance the tetrode stepwise along the track to sample the EAPs in multiple locations and to apply our recently developed cell localization method, 3D dipole characterization (Mechler and Victor 2011), to these recordings. With this tool, we were able to quantify the recording characteristics of tetrodes and gain insight into the properties of cortical neurons.

We have found that the recording volume (radius $\approx 100 \mu\text{m}$) of a stationary tetrode was much larger than its most frequently quoted antecedents ($\approx 60 \mu\text{m}$) (Gray et al. 1995; Henze et al. 2000; Maldonado et al. 1997; Seshagiri and Delgutte 2007), that within this volume the isolation sensitivity was approximately homogeneous and the isolated fraction of neurons small ($\approx 0.3\%$), and that the neurons could be localized with a precision that was much smaller (radius $\approx 50 \mu\text{m}$) than the entire recording volume. This improved precision for localizing a cell requires that it is recorded by the tetrode in more than one position. Pointing to a promising future application, we reconstructed the position of recorded neurons along the electrode track to highlight the potential utility of dipole localization for studies of local circuit physiology. One finding was surprising; the equivalent dipole had a strong tendency to point toward the recording probe. As we discuss below, this suggests that it is not the entire dendritic arbor but rather a local lobe that accounts for the essence of the neuron-probe interaction.

This local lobe viewpoint proves helpful in interpreting a large number of observations, including our dipole characterization results. Therefore, we discuss it first and then turn to our specific findings related to the recording volume and spatial isolation characteristics of tetrodes. These characteristics, which are crucial for the interpretation of cortical extracellular physiology, are difficult to estimate, may strongly depend on the method of assessment, and can vary, even for the same

probe, with the type of brain tissue sampled. Thus, the next major portion of the DISCUSSION details the limitation of our approach and results, and with these in mind we compare our results with those obtained by other investigators.

The Equivalent Dipole

The local lobe interpretation. We find that the moment vector of the equivalent dipole tends to point toward the probe. This is at first surprising, because it is not what one would expect from the standard "far-field" interpretation of the equivalent dipole (in which the moment vector is fixed in space by the morphology of the neuron independent of the direction to the probe). But it does make sense once we recognize that the probe is not in fact in the far field. Rather, the probe tends to pick up activity in the nearest lobe of the soma-dendritic arbor (highlighted in Fig. 8). Since the dendritic arbor of most cortical cells tends to have an approximate radial symmetry (spherical, cylindrical, or that of a flattened ellipsoid; see e.g., Sholl 1953), then no matter what direction the probe approaches, the nearest lobe of the arbor will be oriented from the soma toward the probe. In terms of cellular geometry, this lobe, the local lobe, is understood to be a portion of the dendritic tree

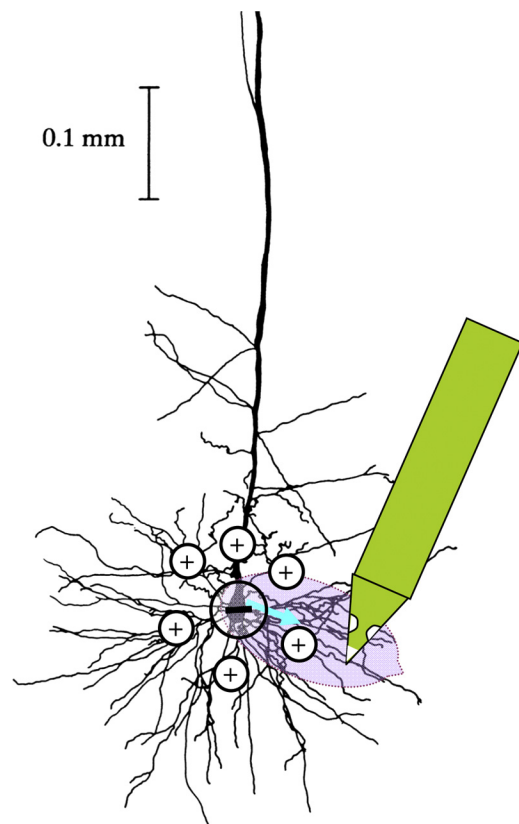


Fig. 8. Interpretation of the equivalent current dipole of a pyramidal cell. The dipole is determined for the peak time of action potential. Its moment vector (blue arrow), oriented by definition from sink (-) to source (+), tended to point away from the soma and toward the probe. This suggests that our dipole localization determines the equivalent source of a local lobe of the soma-dendritic arbor that is nearest to the probe and thus dominates the local extracellular potential field. This should be largely independent of the relative angle of penetration if the dendritic arbor has an approximate spherical symmetry. The (cropped) image of the layer 5 pyramidal cell is used here for illustration only. It is reproduced, with permission, from Cauller and Connors 1992 © (Oxford Academic Press).

whose trunk is one of the primary dendrites anchored at the soma (including but not limited to the primary apical dendrite).

This interpretation also accounts for the scatter of angles between the dipole direction and the cell-probe direction (Fig. 6, *B* and *C*), since the angular scatter we measure experimentally is consistent with the known geometry of cortical neurons. To see this, we use a quantified feature of neuronal geometry, the number of primary dendrites, to estimate the angular subtense of a typical local lobe. The number of primary dendrites in the pyramidal cells (and the spiny stellate cells) of the visual cortex is highly conserved across species; from rodents to primates, it is $n = 6.0 \pm 2.5$ (Sholl 1953; Elston and Rosa 1997; Larkman 1991). Assuming that each of these dendrites occupies the same volume of space, the solid angle occupied by each local lobe is given by $\Omega = 4\pi/n$. Standard solid geometry relates this solid angle to the apical half-angle θ of its cone: $\theta = \cos^{-1}(\Omega/2\pi) = \cos^{-1}(1 - 2/n)$, i.e., $\theta = 50 \pm 10^\circ$ for $n = 6.0 \pm 2.5$. As seen in Fig. 6*B*, this apical half-angle corresponds to the maximum angle between the radial axis of the nearest lobe (i.e., the dipole direction) and the cell-probe axis we observe in the data (Fig. 6, *B* and *C*). Thus, the local lobe interpretation is consistent with an anatomic interpretation of the data in Fig. 6, *B* and *C*, the moment vectors trace the solid angle of the average local lobe of dendrites on the typical visual cortical neuron that our tetrodes isolate.

The current contributions of the local lobe are likely to be dominated by the soma compartment and the trunk or root segment of the primary dendrite. At peak action potential time, large inward Na^+ currents make the soma region of the neuron act as the dominant sink ($-$), and although all dendrites play the role of the (distributed) current source ($+$), only the potential contributions from the currents in the nearest large dendrites of the arbor are large enough to register at the probe. We can estimate the effective sink-source separation from elementary biophysical principles using the notion of a length constant from cable theory. Pettersen and Einevoll (2008) analyzed the AC length constants for ball-and-stick model neurons. Assuming realistic soma diameter and stick lengths of a few hundred micrometers (basal dendrites of neurons in the cortex are about this long), they calculated a $\approx 50\text{-}\mu\text{m}$ length constant at 1 kHz (the temporal frequency characteristic of action potentials). There are two features of real neurons that will tend to make the effective sink-source separation on the local lobe shorter than this. First, the real dendrites are branching trees, not sticks, and currents flowing into the side branches accelerate the rate of current loss in the radial direction away from the soma, making the length constant genuinely shorter. Second, the dendritic arbor on a real neocortical neuron has many lobes, each corresponding to one primary dendrite, and because of symmetry considerations the superimposed fields of all the other lobes together act to weaken the field of the local lobe at hand. This makes the length constant of the effective or equivalent dipole of the local lobe appear even shorter than it is. Thus we think that the characteristic spatial separation of the effective sink and source currents of the local lobe is short, at most a few multiples of $10\ \mu\text{m}$.

We emphasize that this notion is quite distinct from the equivalent dipole of far-field approximation of the whole pyramidal cell. The latter is the sum of all local lobe dipoles, of which the dominant one aligned with the apical dendrite

emerges only at long ranges. The “long-range” regime refers to distances that are several times greater than the effective separation of all sources and sinks, not just the source-sink pair within a local lobe. Thus the far-field approximation is relevant only at a distance of several hundreds of microns from the cell, relevant to EEG and perhaps to local field potential studies but beyond the range of tetrode recording.

Two previous studies support and refine this picture. Pettersen and Einevoll (2008) simulated cable models of cortical pyramidal neurons with realistic geometry and passive membranes; they found that the EAP measured in the 20- to 200- μm range in the direction orthogonal to the apical dendrite will have a dominant dipole component whose moment is oriented in the same direction. Also consistent with the above notions, Gold et al. (2007), using realistic membrane conductances and geometry, found that the current contributions from the nearest dendritic compartments dominate the EAP. Moreover, because the active Na^+ currents of spike generation are likely concentrated in the perisomatic region, the currents on the more distant dendrites would likely share the opposite polarity. Thus, the current source for a locally probed EAP is anticipated to consist of a local lobe of the soma-dendritic arbor anchored to the soma.

The notion of the local lobe is anticipated to be valid only beyond some minimal distance, r_0 , which is comparable with the effective size of the distributed currents that contribute to the dipole. This is consistent with published simulation results from several computational studies of realistic neuron models and our reanalyses (Mechler and Victor 2011 and the supplemental material therein), which consistently demonstrated that there exists a near-field dipole-like regime beyond a minimum distance, $r_0 \approx 30\text{-to-}50\ \mu\text{m}$, extending to $200\ \mu\text{m}$ and beyond. The critical distance, r_0 , is larger for larger neurons (for pyramidal cells in rodent hippocampus $r_0 \approx 20\text{-}30\ \mu\text{m}$, in cat or monkey V1, $r_0 \approx 30\text{-}50\ \mu\text{m}$) or when the active currents of the neuronal action potential generator are more spread out in the dendrites. A rule of thumb is that r_0 , the beginning of the dipole regime, is about four times the soma radius, i.e., $r_0 \approx 4r_{\text{soma}}$ (Rall 1962).

From the point of view of localization of a neuron via its EAP, our simulations (Mechler and Victor 2011 and the supplemental material therein) indicate that a dipole model applied to a realistic distributed source can recover the location of the source provided that $r > r_0$. Those simulations also indicated the procedure tended to slightly ($\approx 10\text{-}15\%$) overestimate source distance, which our estimate of the recording radius is expected to inherit. On the other hand, the biophysical notion of the local lobe may suggest that by associating the soma with the locus of the optimal dipole (a point dipole) we underestimate the soma-probe distance by one-half the characteristic length of the effective biophysical dipole. As mentioned above, the characteristic spatial separation of the effective currents, sink at the soma, source somewhere on the primary dendrite, is likely capped by r_0 , so this bias is probably $< r_0/2$. The above validates the dipole source model for cell localization, even though it represents only a part of the neuron.

As an alternative to the local lobe interpretation (in which the effective dipole depends on the position of the probe) of the finding that the dipole tends to point toward the probe, one might consider an interpretation in which the dipole is fixed to

the cell. According to this alternative interpretation, the bias in the measured dipole directions is simply due to recording only from the cells that are approached from the direction of that fixed dipole (the lead fields of the tetrode would be insensitive to a cell positioned along the orthogonal directions, because the probe would be near the null plane of the dipole of the cell). This, however, is not consistent with our data or known anatomy, as we detail here. First, consider that, conceivably, data similar to Fig. 6 could also arise from encounters with neurons that have fixed equivalent dipoles, but these are randomly oriented; such a distribution could be expected for the weak far-field dipoles of stellate neurons. However, even if the same dipoles prevailed in the near-field approximation for stellate neurons, this scenario could apply only to cells recorded in the granular layers, but those could constitute only a minority of our cortical sample. Next, consider a scenario concerning pyramidal cells, the class containing the majority of cortical neurons. The dominant, apical dendrites are approximately parallel and orthogonal to the laminar planes of cortex, and they determine the far-field dipole; let's assume that in this scenario they prevail in determining the equivalent dipole in the near-field approximation as well. This scenario should result in a sample of isolated neurons in which both the recovered cell locations and the dipole moments were biased by an angle (with respect to the probe axis) that is equal to the penetration angle (with respect to the apical dendrites). Thus, recovered dipoles would tend to point to the probe only in the specific case when the probe penetration was nearly aligned with the apical dendrites, i.e., very close to orthogonal to the laminar plane. But in that case probe sensitivity would be greatest immediately below the tip, resulting in a sample heavily biased for locations immediately below the tip. Our penetrations were along sharp but nonzero angles ($\sim 15\text{--}30^\circ$) with respect to the cortical surface normal, and yet we see no such position bias in our data. Thus neither scenario is consistent with our data.

We mention that we did not record the precise value of the angle of our oblique penetrations (they were in the approximate range of $15\text{--}30^\circ$). Although the results presented here do not depend on it, knowledge of the penetration angle is obviously crucial for any application of dipole localization that aims at studying the functional microarchitecture of cortex.

The local lobe interpretation of the equivalent dipole together with the minimum distance for the dipole regime offers a concise account for a number of otherwise puzzling observations in our data in addition to the main finding that the equivalent dipole tends to point toward the probe. It also provides some guidelines for the implementing and interpreting this approach. We highlight these in the following.

The cell-probe distance where isolation likelihood dips and peaks. The dipole localization will overestimate the distance to cells encountered by the probe at very short distances ($r < r_0$), yielding an apparent distance larger than r_0 (supplemental material of Mechler and Victor 2011). This systematic error will result in an empirical volume-corrected distribution of cell-probe distances (Fig. 4A, bottom) that is impoverished for distances $r < r_0$ and has a local maximum at $r > r_0$ (due to the erroneously projected short-distance subset). We see this in our data: a dip below $50\ \mu\text{m}$ and a small peak near $70\ \mu\text{m}$ (Fig. 4A, bottom).

The cell-probe distance where fitting error peaks. Since the local maximum in the isolation likelihood of cell-probe distances at $r > r_0$ results from neurons in which the local lobe approximation fails, the dipoles fit to the EAPs of these neurons should have the largest MSEs. Indeed, we see the largest fitting errors in a handful of cells localized near $70\text{--}80\ \mu\text{m}$ (not shown).

No polarity inversion in EAP. A dendritic arbor of approximate radial symmetry, essentially a radial array of lobes, predicts that the probe will see no polarity inversion of the EAP as the electrode is advanced beyond the neuron. Rall's (1962) classic analysis of passive cable models predicted this phenomenon, and it is corroborated by a common anecdotal experience of most investigators of most cortices. In contrast, polarity inversion of the EAP becomes frequently detectable in the CA1 area of hippocampus (Csicsvari et al. 2003), where dendrites of the pyramidal neurons have a characteristically anisotropic organization.

Dipole moment larger for local lobe than the whole cell. The magnitude of the equivalent dipole corresponding to the whole neuron in the far-field approximation (Kyuhou and Okada 1993; Murakami and Okada 2006) appears to be smaller than the dipole we identified and associated with a single local lobe. This is not a contradiction because the far-field dipole results from summing the contributions of each local lobe of an arbor of approximate radial symmetry, and contributions from opposing lobes should mostly cancel (by symmetry considerations, the resulting far-field dipole should align with the relatively larger apical dendrite).

Linear span of cell detection may be shorter than recording radius. If, as informal observation about the typical cell morphology suggests, the dendritic arbor is somewhat flattened, the length of detectable signals along most passages will be expected to be shorter than the distance to the cell (in contrast, they are expected to be comparable for random passages through a perfect sphere). This expectation is borne out by our data; average passage length was $54\ \mu\text{m}$ (see METHODS), and average cell-probe distance was $\approx 100\ \mu\text{m}$ (Fig. 4A, top).

Recording volume may inherit anisotropies from the neural substrate. In V1, we found that the recording volume is approximately isotropic. The local lobe viewpoint predicts that in a brain area in which the cellular morphology is highly anisotropic, the recording volume will inherit this anisotropy because some directions of probe approach will be more effective than others. One obvious example is the organization of basal dendrites in the pyramidal cell of CA1 of the hippocampus in a cone that is directed away from stratum pyramidale, the layer of somata, to clear the room for the densely packed cell bodies. This organization results in a reinforcement of current contributions from each lobe of the basal arbor, resulting in a net current flow aligned with the apical dendrite. Consistent with this axial dominance, Henze et al. (2000) measured a $R = 50\ \mu\text{m}$ recording radius in the plane of stratum pyramidale of CA1, but these same authors found evidence that the EAP spread was larger in the orthogonal CA1 direction (Henze et al. 2000; see *Recording radius scales with source size* below).

Dipole moment of local lobe is unsuited to classify neurons. The equivalent dipoles determined by source modeling are not likely to be cell type specific, since they depend on the encounter between the probe and the local lobe rather than the

overall geometry of the dendritic tree. As a consequence, the distribution of dipole moment magnitudes cannot be expected to reflect anatomically or physiologically defined cell classes. Indeed, we discerned no distinct modes in the moment distribution in visual cortex.

Source model support for spatially extensive EAP sample. The notion of local lobe highlights the importance of keeping the spatial EAP sample relatively local, i.e., within a small solid angle viewed from the soma, to support the underlying dipole model. We met this criterion in our tetrode experiments because the average passage length and cell-probe distance (see above) together defined a small angle $[(2\pi/6)^2 \text{ sterad}]$. Use of a sample that extended much beyond this could emphasize the distributed nature of the source and would require a source model more complex than the single dipole. This issue may arise with spatially extensive silicon polytrodes (Blanche et al. 2005; Csicsvari et al. 2003) that can pick up very small signals over large distances by taking advantage of spike-triggered averaging.

Sampling EAP at peak time is optimal for dipole localization. Dipole localization is best done from estimates taken before or at peak EAP time, when the equivalent dipole is both the largest and its location is most well determined. This is because the second half of the action potential waveform is dominated by potassium currents, which are not as well confined to the perisomatic region as the sodium currents that dominate the first half (Gold et al. 2006).

The Recording Radius and Volume of Tetrodes

The Thomas tetrode. After correcting for the 10–15% excess by which the dipole model tends to overestimate source distance (Mechler and Victor 2011), and estimating separately for different contact separation (Δs) on the Thomas tetrodes, the R_{50} recording radius was ≈ 80 – $85 \mu\text{m}$ for the smaller and intermediate tetrodes ($\Delta s = 29 \mu\text{m}$ and $\Delta s 38 \mu\text{m}$, respectively) and ≈ 95 – $100 \mu\text{m}$ for the larger tetrode ($\Delta s = 45 \mu\text{m}$). These ranges of tetrode sensitivity are generally consistent with the characteristic linear span (can be $>200 \mu\text{m}$) over which polytrodes reportedly register signals from cortical single units (Blanche et al. 2005; Drake et al. 1988) but remain significantly larger than the ≈ 50 - to $70\text{-}\mu\text{m}$ recording radii reported for twisted wire tetrodes (Gray et al. 1995; Henze et al. 2000; Maldonado et al. 1997; Seshagiri and Delgutte 2007). There are several reasons the estimates can differ; the most important ones are difference in source model type, probe size (contact separation), and neuron size. We discuss these separately below.

Monopole models lead to localization bias. Perhaps because of its simplicity, several studies have used a monopole source model to localize neurons from extracellular recordings (Chelaru and Jog 2005; Lee et al. 2007; Somogyvari et al. 2005). However, as discussed above (*The local lobe interpretation*), the field around a neuron beyond a minimum r_0 is accurately approximated by a dipole rather than a monopole. For a cell at $r > r_0$ distance from the probe, the monopole model will underestimate its distance by about 50% (Lee et al. 2007; also see 2nd supplemental material in Mechler and Victor 2011). The absolute localization error at $r > r_0$ can be large enough to be comparable with the recording radius of the probe.

Even for probe positions very close to the cell ($r < r_0$, where the dipole model fails), the monopole model may be of some-

what limited accuracy because it alone cannot fully capture the changing rate of potential falloff with distance in the cell vicinity (1st supplemental material of Mechler and Victor 2011). However, these near encounters are likely signified by large EAP amplitudes recorded by the probe, and the absolute error of localization will not be too large ($\approx r_0$).

Recording radius scales with contact separation. Recording radius is expected to depend on contact separation monotonically. Intuitively, reliable single-unit isolation is achieved when a criterion level of relative signal amplitude variation, measured across the probe contacts, is reached. To meet this criterion, a smaller probe would have to be moved closer to the source, where the signal itself is also stronger.

To quantify this, assume that the EAP amplitude, V , of a neuron depends on distance, r , according to a power function, $V(r) \propto r^k$, where the k exponent characterizes the approximate equivalent multipole of the source. As a first approximation, the contact separation, Δs , determines the ΔV voltage difference between the electrode contacts as $\Delta V = \Delta s V'$, where V' is the potential gradient at the location of the probe. Using this equality, the isolation criterion can be formally stated as $\Delta s |V'|/V = \text{const}$. The $|V'|/V$ ratio on the left-hand side can be evaluated from the power function approximation for V : $|V'|/V = k/r$. Substitution of this into the isolation criterion, followed by rearrangement of variables, yields $r_c \propto \Delta s/k$. This means that a smaller (larger) probe has to be moved closer (farther) to the cell in proportion to the change in the contact separation, i.e., $r_c \propto \Delta s$.

We emphasize that this analysis refers to probe separation, not contact size. The latter has very little influence on the recording radius [see Moffitt and McIntyre (2005) and the lead-field analysis in the accompanying paper (Mechler and Victor 2011)].

In practice, noise and other factors may blur this dependence. In these experiments, we used three different tetrodes whose typical contact separations (the mean of s_{CE} and s_{EE} in Table 1) were 29, 38, and 45 μm . We found the expected proportional increase in recording radius for the comparison between the two largest probes (a factor of 1.2; see *Sample Pooling*) but no significant difference for the comparison for the two smallest probes (a factor 1.3 size difference). The failure of our data to lend consistent support for the expected proportionality could be a result of small sample sizes ($n \approx 10$) and confounds between tetrode size and experimental variability (different animals, sampled cortical areas, etc).

Twisted wire tetrodes are smaller than the Thomas tetrodes we used, and it is possible that this difference contributes to the difference in the reported values of recording radii. The sample-weighted average of the mean contact separation on our tetrodes was 37 μm , and the nominal contact separation of the twisted wire tetrodes is 12–15 μm (Csicsvari et al. 2003; Gray et al. 1995; Henze et al. 2000; Jog et al. 2002), but because of wire splaying at the tip the true contact separation is more like 20–30 μm (Chelaru and Jog 2005; Jog et al. 2002). Thus, according to the above analysis, the difference in contact separation would produce a recording radius for a twisted wire tetrode that is smaller than that of a Thomas tetrode by a factor of 0.5–0.8.

Since Gray et al. (1995) recorded from cat area 17, we can make a direct comparison, and it supports this analysis. Gray's $R_{\text{exp}} \approx 65 \mu\text{m}$ recording radius is defined in cat area 17, and

near their noise threshold, and was obtained by triangulation based on a phenomenological approximation of extracellular potentials (Bartho et al. 2004; Buzsaki 2004; Gray et al. 1995; Maldonado et al. 1997; Seshagiri and Delgutte 2007). The value of R_{exp} reported by Gray et al. is consistent with a $\Delta s = 25 \mu\text{m}$ effective contact separation on their wire tetrodes (Chelaru and Jog 2005; Jog et al. 2002). (See details of the calculations involved in our supplemental material; Supplemental Material for this article can be found online at the *Journal of Neurophysiology* web site.) We compare these measurements of the Gray et al. study with our $R_{\text{cat}} \approx 124 \mu\text{m}$ for the subset of data we recorded in cat area 17 (R_{cat} is here defined by the most distant cell among the total of 10 cells recorded, and the tetrode used to collect this sample had $\Delta s = 45 \mu\text{m}$ contact separation). The $45/25 \approx 1.8$ ratio of contact separations is in remarkable agreement with the $124/65 \approx 1.9$ ratio of recording radii. The supplemental material presents a further comparison with Gray et al. 1995 based on applying their triangulation method to our data. Similarly good agreement is reached, providing further evidence that 1) recording radius scales with contact separation and 2), in twisted wire tetrodes, splaying increases the effective contact separation, which is necessary to take into account for source localization.

Finally, we mention that the triangulation method used by Gray et al. (1995) provides further evidence for the utility of the equivalent dipole model and of the power law approximation used above to relate recording radius to contact separation (see supplemental material for further details). In brief, when a power law r^{-k} is locally fit by the exponential falloff $\exp(-r/\lambda)$ used by Gray (1995), the apparent length constant is given by $\lambda(r) \approx k^{-1}r$ or $k \approx r/\lambda$ (this is Eq. 14 in the supplemental material, and it is readily obtained by equating the derivatives of the 2 functions). Derived from Gray's data or from ours, the ratio r/λ is very close to 2, indicating a dipolar power law (a monopole corresponds to $k = 1$). Thus, although the two types of tetrodes are significantly different in size and thus must be used at significantly different distances from the cells, a dipole regime describes the extracellular action potentials of cat V1 neurons in both ranges.

Note that impedance does not play a role in determining recording radius. The reason for this is that most of the recording noise comes from background neural activity, not instrumentation, so changing the impedance simply results in an equal rescaling of signal and neural noise. For microelectrodes, impedance, which is inversely related to contact area, is often used as an indirect measurement of tip size, but it is the tip size, not the impedance per se, that determines cell isolation (e.g., see Robinson 1968) and recording radius. For tetrodes, the key geometric factor (as indicated above) is the contact separation.

Recording radius scales with source size. In technically difficult in vivo dual recordings carried out in hippocampal CA1 pyramidal neurons in the anesthetized rat, Buzsaki's team (Henze et al. 2000) directly measured the recording radius of their twisted wire tetrodes. Defining the recording radius at the signal criterion of extracellular single unit isolation, they measured $R_{\text{CA1}} \approx 50 \mu\text{m}$. Consistent with a dependence on probe size, this is a much smaller radius than our similarly defined estimate for the larger Thomas tetrodes ($R_{95} \approx 120\text{--}140$, in cat or monkey V1, depending on species). However, Henze et al.'s R_{CA1} is also significantly lower than Gray et al.'s $R_{\text{exp}} \approx 65 \mu\text{m}$

estimate (in cat V1), even though the wire tetrodes used by the two groups were the same type and presumably the same size. We show below that almost all of this $\approx 30\%$ difference can be explained by a difference in source size (i.e., strength) and does not require an explanation based on difference in the methods of estimation.

From very early on, there was experimental evidence that recording radius depended on the source size of neurons; Humphrey (1978) argued that the very wide range (40–300 μm) over which his single microelectrodes could isolate pyramidal cells in the primate motor cortex implied size heterogeneity of the neuron population. Cell size correlates with equivalent current source size (Gold et al. 2007), and cable models predict that the equivalent current source size is proportional to the total cross-sectional area of the main dendrites (Pettersen and Einevoll 2008). This is an especially useful rule of thumb among classes of neurons that have similar overall shape. Because recording radius is determined by the distance at which the measured voltage falls to a criterion level, say V_c , the same probe may have a smaller recording radius when recording from populations of smaller neurons. Specifically, if the EAP amplitude, V , depends on distance, r , according to a power function, $V(r) \propto pr^{-k}$, the recording radius, defined for a criterion EAP amplitude, V_c , will scale as $R \propto (p/V_c)^{1/k}$, where p is the current source strength.

Making use of Pettersen and Einevoll's conclusion, we estimate the relative strength of p from the cross-sectional area of the main dendrites, and in turn we estimate this from anatomic measurements. The data (means \pm SD) critical to our specific comparison include soma radius, which is $7.8 \pm 1.0 \mu\text{m}$ in rat CA1 (Altemus et al. 2005; Ishizuka et al. 1995) vs. $10 \pm 2 \mu\text{m}$ in cat V1 (Sholl 1953), and the number of primary (basal + apical) dendrites, which is 4.8 ± 1.1 in rat CA1 (Altemus et al. 2005; Ishizuka et al. 1995) vs. 6.0 ± 2.5 in cat V1 (Sholl 1953). Using these values (and standard error propagation), we estimate that the relative fraction, rat CA1 vs. cat V1 pyramidal cells, of the soma radius is $7.8/10 = 0.78 (\pm 0.18)$, of the soma surface area is $(7.8/10)^2 \approx 0.61 (\pm 0.28)$, of the number of primary dendrites is $4.8/6.0 \approx 0.80 (\pm 0.38)$, and, assuming that the size of the initial dendrites scale with the soma, of the total cross-sectional area of the initial dendrites is $0.61 \times 0.8 = 0.49 (\pm 0.34)$. Thus, according to the above rule of thumb, the size of the equivalent current source of pyramidal cells in rat CA1 is expected to be $0.49 (\pm 0.34)$ of that in cat V1. The $R \propto (p/V_c)^{1/k}$ formula, used with $k = 2$ for a dipole approximation to the EAP of pyramidal neurons in both cortices, in turn predicts that the recording radius of the same tetrode in CA1 is $\approx \sqrt{0.49} = 0.70 (\pm 0.25)$ of the radius in V1 [if the initial dendrites did not scale with the soma, the predicted fractional source size would be $\sqrt{0.80} = 0.89 (\pm 0.21)$]. The measured 0.77 ratio of Henze et al.'s $R_{\text{CA1}} = 50 \mu\text{m}$ estimate in rat CA3 over Gray et al.'s $R_{\text{exp}} = 65 \mu\text{m}$ estimate in cat V1 is near the predicted mean and well within the predicted range.

Most of this difference is attributable to a difference in functional cell morphology between hippocampus and striate cortex rather than a species difference. Generally, neurons in homologous cortical area of different species have similar size and morphology, but pyramidal cells in different cortices of the same species can have very different size, morphology, and spatial organization. For example, the soma radius in V1 pyramidal cells is comparable ($\approx 10 \pm 2 \mu\text{m}$) in rat (Larkman

and Mason 1990) and cat (Sholl 1953), and the radius in CA1 pyramidal cells is only slightly smaller in rat (7.8 μm) than in monkey (9.5 μm) (Altemus et al. 2005). However, across distinct visual cortical areas of the monkey, soma diameter and basal dendritic field area of layer 3 pyramidal cells undergo a doubling from area V1 to area TE (Elston et al. 1999).

Next, we address a possible concern. Henze et al. (2000) routinely recorded larger EAP amplitudes (median $>200 \mu\text{V}$) than was customary in our V1 recordings ($\approx 100 \mu\text{V}$), even though the V1 cells are larger and their equivalent current sources are stronger. Most likely this is because to be able to isolate a CA1 cell, the smaller wire tetrodes must move closer to it [to within 20 μm (Buzsaki 2004)] than the larger Thomas tetrode could or would need to (see the preceding section). Further raising the minimum required signal level is a higher level of background activity in CA1 than V1; in hippocampal CA1, neuronal packing density is very high [$\approx 0.3 \times 10^6/\text{mm}^3$ in rat CA1 (Boss et al. 1987) vs. $\approx (0.05 \pm 0.01) \times 10^6/\text{mm}^3$ in cat V1 (Beaulieu and Colonnier 1987)], and neuronal spiking activity is frequently synchronized with the local field (Csicsvari et al. 1999). In turn, the high cell-packing density makes moving closer to a CA1 cell body easier, as does the special anisotropic cell morphology (see more on anisotropy below).

We remind the reader that there exists a proximal bound on the dipole regime, i.e., a radius, r_0 , from the soma, within which the dipole approximation is not valid. In CA1, we estimate that $r_0 \approx 30 \mu\text{m}$, corresponding to an (negative peak) EAP amplitude of $\approx 150 \mu\text{V}$. To estimate r_0 , we use the rule of thumb that the proximal bound is about four times the soma radius, i.e., $r_0 \approx 4r_{\text{soma}}$ (Rall 1962); with $r_{\text{soma}} \approx 8 \mu\text{m}$ in rat CA1 pyramidal cells (Altemus et al. 2005; Ishizuka et al. 1995), $r_0 \approx 30 \mu\text{m}$. To estimate the corresponding EAP amplitude, we use the $\sim r^{-2}$ dependence of EAP on distance in the dipole range to extrapolate from Henze et al.'s (2000) measurements; the amplitude is $\approx 60 \mu\text{V}$ (the isolation threshold) at $R \approx 50 \mu\text{m}$ (the recording radius), and thus by multiplying 60 μV by a factor of $(R/r_0)^2 \approx 2.5$ we get $\approx 150 \mu\text{V}$ at r_0 . Thus, the largest EAPs typically recorded (median $>200 \mu\text{V}$) may correspond to neurons that are just below the critical radius, r_0 , at which the dipole regime breaks down.

In contrast, we anticipate that the dipole regime nearly always applies to our V1 recordings. Although we recorded from larger neurons than those in CA1 [$r_{\text{soma}} \approx 10 \mu\text{m}$ in cat V1 (Sholl 1953)], we used a larger tetrode and thus were able to isolate the very large majority of the neurons at distances ($r > r_0 \approx 4r_{\text{soma}} \approx 40 \mu\text{m}$) where the dipole regime is expected to hold.

Finally, we mention that with regard to some features of histology, monkey V1 is more similar to rat CA1 than to cat V1; neurons are smaller [soma radius is $\sim 7 \mu\text{m}$ on average (Elston and Rosa 1997; Fries and Distel 1983)], and with an average numerical density of $n \approx 0.12 \times 10^6/\text{mm}^3$ (Cragg 1967; O'Kusky and Colonnier 1982) they are packed two to three times more densely than in cat V1. Despite these differences between cat and monkey V1, the case for a larger equivalent current source size and, in turn, a larger recording radius in cat is weak. This is because in other key features the similarity between cat and monkey is strong; in both species, V1 neurons have very similar number of primary dendrites, ≈ 6 (Elston and Rosa 1997; Kossel et al. 1995; Sholl 1953), and the

laminar variation is more than two- to threefold in soma volume (Sherwood et al. 2003) and packing density (Beaulieu and Colonnier 1987) (in contrast, rat CA1 has only a single pyramidal layer and a consistently five- to sixfold higher density than cat V1). So even if there was a true underlying species-specific difference in average neuronal source size, samples of limited size may be consistent with the assumption that the equivalent current source of the average V1 neuron is not significantly different in monkey and cat. In our data, the difference in probe size alone was sufficient to account for the different recording radii we measured in cat ($\approx 124\text{-}\mu\text{m}$ recording radius for 45- μm contact separation) and monkey ($\approx 94\text{-}\mu\text{m}$ recording radius for 32- μm contact separation), just as it did compared with Gray et al.'s results ($\approx 65\text{-}\mu\text{m}$ recording radius for $\approx 25\text{-}\mu\text{m}$ contact separation); the ratio of recording radius to contact separation is between 2.5:1 and 3:1 and is conserved across species and laboratories.

The Isolated Fraction

The isolated fractions reported here and elsewhere for various electrode types are strikingly lower than the spiking fraction implicated by the experiments using in vivo 2-photon Ca-sensitive dye imaging of visually stimulated V1 neurons (Ohki et al. 2005). The difference begs for an explanation, but in the absence of hard quantitative evidence such an account is necessarily speculative. To begin, we first consider the distinctions between the notions of the Ca-active fraction, the spiking fraction, and the isolated fraction. Ca-sensitive dye imaging data assess the Ca-active fraction, which can be as high as 60–90% (Ohki et al. 2005; Ohki et al. 2006). The Ca-active fraction could overestimate the spiking fraction if control for some experimental artifacts [e.g., for calcium signals from glia, light scatter from cells in depth and the neighboring neuropil (Ohki et al. 2005)] was incomplete or if accumulated contributions to the somatic calcium concentration from slow, compartmentalized, or otherwise negligible processes [e.g., synaptic, storage, etc; for a list see Cossart et al. (2005)], which the low frequency sampling would not allow to discriminate from spike contributions, became significant under the relatively prolonged stimulation. Thus the true spiking fraction in the intact animal may be lower than 60%, but the difference, although hard to quantify, is very likely less than an order of magnitude.

In contrast, the isolated fraction assessed by a recording electrode is likely an underestimate of the spiking fraction in intact animals, also because of factors that are hard to quantify. First, the spiking fraction in the brain probed by a recording electrode could be significantly lower than the spiking fraction in the intact brain because the insertion of the probe could cause tissue damage, including 1) the physical destruction of a fraction of potentially spiking neurons; 2) local anoxia resulting from compression and breakage of blood vessels and the dense capillary plexi (Harrison et al. 2002); 3) damage to neurons caused by the loss of the blood-brain barrier and release of toxic blood-borne chemicals; and 4) stretching and severing of dendrites and afferent axons, leading to a loss of inputs to surviving cells and altering of electrolyte compositions, as well as triggering intracellular responses to damage that might include being electrically silent. In addition to this, there is 5) a complex cascade of posttraumatic immunological

responses that further reduce local neural densities and insulate the electrode in chronic recordings (Ward et al. 2009). Around the probe, 6) the formation of partial fluid shunts reduce electrode sensitivity. In addition, 7) damaged neurons and glia could be a source of a diffusing inhibitory substance.

Second, the isolated fraction assessed from single-unit recordings could well underestimate even the actual experimentally compromised spiking fraction because the probe may be insensitive to a subset of the spiking neurons for any of the following reasons. 1) It is suspected that a large subset of the actual spiking neurons are spiking too infrequently [for a review of the supporting earlier experimental evidence as well as potential theoretical reasons, see, e.g., (Olshausen and Field 2005)] and thus issue too few spikes in a finite experiment to allow reliable isolation. Note that a strongly skewed firing rate distribution, which likely gives rise to a strong experimental sampling bias that is thought to characterize electrode recordings, can be consistent with a large Ca-active fraction. 2) The recording probe cannot resolve multiple single units, especially those with relatively small EAP amplitudes [this possibility was highlighted by Blanche et al. (2005)]. 3) Tissue conductivity may increase with increased neural activity [such an effect was measured in the hippocampus (Lopez-Aguado et al. 2001)], decreasing the recording radius of a probe; failing to take this into account would lead to an underestimate of the spiking fraction. 4) The probe geometry may have probe-specific spatial variation of selectivity, i.e., a reduced sensitivity to neurons located in certain spatial directions (the variation with 3-fold symmetry of azimuth sensitivity of the tetrahedral tetrode is a mild example). These factors (and possibly others) could substantially lower the isolated fraction below the true spiking fraction.

In summary, there appears to be a difference of approximately two orders of magnitude between the number of visually responsive single neurons that are identified by two-photon calcium imaging and tetrode recordings. Although damage caused by tissue penetration is undoubtedly an important factor, there are many other factors that are equally difficult to quantify that likely contribute. A complete understanding of this gap is clearly important but requires extensive further investigation along multiple avenues.

Future Work on Ensemble Configuration and Functional Microarchitecture

A prime application of dipole localization of cortical neurons would be to aid studies of functional organization of cortical circuits on the scale of a few multiples of a cortical microcolumn. Our results reveal a recording radius that is larger than previously thought, a factor that may have confounded earlier microelectrode studies of the spatial organization of single-neuron receptive field properties in sensory cortex. This new recognition warrants extra caution when interpreting earlier studies that reported evidence against tight clustering (Gegenfurtner et al. 1996; Lennie et al. 1990; Leventhal et al. 1995; Yen et al. 2007). But this confound could affect even those studies that reported evidence supporting fine-scale cortical organization (DeAngelis et al. 1999; Gallant et al. 1996; Hetherington and Swindale 1999; Hubel and Wiesel 1974; Ohki et al. 2005; Yao and Li 2002; Yen et al. 2007).

More recently, synchronous ensemble activity and, more generally, the pattern of coactivation of a local ensemble of neurons and its dependence on distances among the neurons has been a focus of investigation (e.g., Ohiorhenuan et al. 2010; Schneidman et al. 2006; Shlens et al. 2006). Local ensemble activity and spatial configuration are also cardinal ingredients of large-scale realistic cortical models that have been developed as critical data have become available (e.g., Tao et al. 2004; Zhu et al. 2009). These lines of investigations would greatly benefit from experimental techniques that can combine physiological data with the reconstructed anatomic configuration of the ensemble. Multiarray recordings (which enjoy a number of advantages over tetrodes; for a discussion, see Mechler and Victor 2011), when coupled with model-based source localization, as described here, can fill this important niche.

ACKNOWLEDGMENTS

We thank Mike Repucci for help with the data collection; Dirk Hoehl and Thomas Recording for their consistently reliable tetrodes; Dr. Stephen B. Doty and Tony Labassiere of Analytical Microscopy Core Facility, Hospital for Special Surgery, New York, NY, for the scanning electron microscopy; and Drs. Partha Mitra and Alexander Polyakov for stimulating early discussions and introducing the use of Femlab.

GRANTS

This work was supported by National Institutes of Health Grant EY9314 (J. Victor, F. Mechler).

DISCLOSURES

No conflicts of interest, financial or otherwise, are declared by the authors.

REFERENCES

- Altemus KL, Lavenex P, Ishizuka N, Amaral DG. Morphological characteristics and electrophysiological properties of CA1 pyramidal neurons in macaque monkeys. *Neuroscience* 136: 741–756, 2005.
- Barber DC, Brown BH. Applied Potential Tomography. *J Phys E Sci Instrum* 17: 723–733, 1984.
- Bartho P, Hirase H, Monconduit L, Zugaro M, Harris KD, Buzsaki G. Characterization of neocortical principal cells and interneurons by network interactions and extracellular features. *J Neurophysiol* 92: 600–608, 2004.
- Baumann SB, Wozny DR, Kelly SK, Meno FM. The electrical conductivity of human cerebrospinal fluid at body temperature. *IEEE Trans Biomed Eng* 44: 220–223, 1997.
- Beaulieu C, Colonnier M. Effect of the richness of the environment on the cat visual cortex. *J Comp Neurol* 266: 478–494, 1987.
- Blanche TJ, Spacek MA, Hetke JF, Swindale NV. Polytrodes: high-density silicon electrode arrays for large-scale multiunit recording. *J Neurophysiol* 93: 2987–3000, 2005.
- Boss BD, Turlejski K, Stanfield BB, Cowan WM. On the numbers of neurons in fields CA1 and CA3 of the hippocampus of Sprague-Dawley and Wistar rats. *Brain Res* 406: 280–287, 1987.
- Buzsaki G. Large-scale recording of neuronal ensembles. *Nat Neurosci* 7: 446–451, 2004.
- Buzsaki G, Kandel A. Somadendritic backpropagation of action potentials in cortical pyramidal cells of the awake rat. *J Neurophysiol* 79: 1587–1591, 1998.
- Callaway EM. Local circuits in primary visual cortex of the macaque monkey. *Annu Rev Neurosci* 21: 47–74, 1998.
- Cauler LJ, Connors BW. Functions of very distal dendrites: experimental and computational studies of layer 1 synapses on neocortical pyramidal cells. In: *Single Neuron Computation*, edited by McKenna T, Davis J, and Zornetzer SF. San Diego, CA: Academic, 1992, p. 199–229.
- Chelaru MI, Jog MS. Spike source localization with tetrodes. *J Neurosci Methods* 142: 305–315, 2005.

- Collins CE, Airey DC, Young NA, Leitch DB, Kaas JH. Neuron densities vary across and within cortical areas in primates. *Proc Natl Acad Sci USA* 107: 15927–15932, 2010.
- Cossart R, Ikegaya Y, Yuste R. Calcium imaging of cortical networks dynamics. *Cell Calcium* 37: 451–457, 2005.
- Cragg BG. The density of synapses and neurones in the motor and visual areas of the cerebral cortex. *J Anat* 101: 639–654, 1967.
- Csicsvari J, Henze DA, Jamieson B, Harris KD, Sirota A, Barthó P, Wise KD, Buzsáki G. Massively parallel recording of unit and local field potentials with silicon-based electrodes. *J Neurophysiol* 90: 1314–1323, 2003.
- Csicsvari J, Hirase H, Czurkó A, Mamiya A, Buzsáki G. Fast network oscillations in the hippocampal CA1 region of the behaving rat. *J Neurosci* 19: RC20, 1999.
- DeAngelis GC, Ghose GM, Ohzawa I, Freeman RD. Functional micro-organization of primary visual cortex: receptive field analysis of nearby neurons. *J Neurosci* 19: 4046–4064, 1999.
- Drake KL, Wise KD, Farraye J, Anderson DJ, BeMent SL. Performance of planar multisite microprobes in recording extracellular single-unit intracortical activity. *IEEE Trans Biomed Eng* 35: 719–732, 1988.
- Eckhorn R, Thomas U. A new method for the insertion of multiple microprobes into neural and muscular tissue, including fiber electrodes, fine wires, needles and microsensors. *J Neurosci Methods* 49: 175–179, 1993.
- Elston GN, Rosa MG. The occipitoparietal pathway of the macaque monkey: comparison of pyramidal cell morphology in layer III of functionally related cortical visual areas. *Cereb Cortex* 7: 432–452, 1997.
- Elston GN, Tweedale R, Rosa MG. Cortical integration in the visual system of the macaque monkey: large-scale morphological differences in the pyramidal neurons in the occipital, parietal and temporal lobes. *Proc Biol Sci* 266: 1367–1374, 1999.
- Emondi AA, Rebrik SP, Kurgansky AV, Miller KD. Tracking neurons recorded from tetrodes across time. *J Neurosci Methods* 135: 95–105, 2004.
- Fries W, Distel H. Large layer VI neurons of monkey striate cortex (Meynert cells) project to the superior colliculus. *Proc R Soc Lond B Biol Sci* 219: 53–59, 1983.
- Gallant JL, Connor CE, Rakshit S, Lewis JW, Van Essen DC. Neural responses to polar, hyperbolic, and Cartesian gratings in area V4 of the macaque monkey. *J Neurophysiol* 76: 2718–2739, 1996.
- Gegenfurtner KR, Kiper DC, Fenstemaker SB. Processing of color, form, and motion in macaque area V2. *Vis Neurosci* 13: 161–172, 1996.
- Gold C, Henze DA, Koch C. Using extracellular action potential recordings to constrain compartmental models. *J Comput Neurosci* 23: 39–58, 2007.
- Gold C, Henze DA, Koch C, Buzsáki G. On the origin of the extracellular action potential waveform: A modeling study. *J Neurophysiol* 95: 3113–3128, 2006.
- Gray CM, Maldonado PE, Wilson M, McNaughton B. Tetrodes markedly improve the reliability and yield of multiple single-unit isolation from multi-unit recordings in cat striate cortex. *J Neurosci Methods* 63: 43–54, 1995.
- Hansen PC, O'Leary DP. The use of the L-curve in the regularization of discrete ill-posed problems. *Siam J Sci Comput* 14: 1487–1503, 1993.
- Harris KD, Henze DA, Csicsvari J, Hirase H, Buzsáki G. Accuracy of tetrode spike separation as determined by simultaneous intracellular and extracellular measurements. *J Neurophysiol* 84: 401–414, 2000.
- Harrison RV, Harel N, Panesar J, Mount RJ. Blood capillary distribution correlates with hemodynamic-based functional imaging in cerebral cortex. *Cereb Cortex* 12: 225–233, 2002.
- Helmholtz H. Ueber einige Gesetze der Vertheilung elektrischer Stroeme in Koerperlichen Leitern mit Anwendung auf die thierisch-elektrischen Versuche (I). *Ann der Phys und Chemie (Leipzig, 3rd Ser)* 89: 211–233, 1853.
- Henze DA, Borhegyi Z, Csicsvari J, Mamiya A, Harris KD, Buzsáki G. Intracellular features predicted by extracellular recordings in the hippocampus in vivo. *J Neurophysiol* 84: 390–400, 2000.
- Hetherington PA, Swindale NV. Receptive field and orientation scatter studied by tetrode recordings in cat area 17. *Vis Neurosci* 16: 637–652, 1999.
- Hubel DH, Wiesel TN. Uniformity of monkey striate cortex: a parallel relationship between field size, scatter, and magnification factor. *J Comp Neurol* 158: 295–305, 1974.
- Humphrey DR, Corrie WS, Rietz R. Properties of the pyramidal tract neuron system within the precentral wrist and hand area of primate motor cortex. *J Physiol (Paris)* 74: 215–226, 1978.
- Ishizuka N, Cowan WM, Amaral DG. A quantitative analysis of the dendritic organization of pyramidal cells in the rat hippocampus. *J Comp Neurol* 362: 17–45, 1995.
- Jog MS, Connolly CI, Kubota Y, Iyengar DR, Garrido L, Harlan R, Graybiel AM. Tetrode technology: advances in implantable hardware, neuroimaging, and data analysis techniques. *J Neurosci Methods* 117: 141–152, 2002.
- Kossel A, Lowel S, Bolz J. Relationships between dendritic fields and functional architecture in striate cortex of normal and visually deprived cats. *J Neurosci* 15: 3913–3926, 1995.
- Kyuhou S, Okada YC. Detection of magnetic evoked fields associated with synchronous population activities in the transverse CA1 slice of the guinea pig. *J Neurophysiol* 70: 2665–2668, 1993.
- Larkman A, Mason A. Correlations between morphology and electrophysiology of pyramidal neurons in slices of rat visual cortex. I. Establishment of cell classes. *J Neurosci* 10: 1407–1414, 1990.
- Larkman AU. Dendritic morphology of pyramidal neurones of the visual cortex of the rat: I. Branching patterns. *J Comp Neurol* 306: 307–319, 1991.
- Lee CW, Dang H, Nenadic Z. An efficient algorithm for current source localization with tetrodes. *Conf Proc IEEE Eng Med Biol Soc* 2007: 1282–1285, 2007.
- Lennie P, Krauskopf J, Sclar G. Chromatic mechanisms in striate cortex of macaque. *J Neurosci* 10: 649–669, 1990.
- Leventhal AG, Thompson KG, Liu D, Zhou Y, Ault SJ. Concomitant sensitivity to orientation, direction, and color of cells in layers 2, 3, and 4 of monkey striate cortex. *J Neurosci* 15: 1808–1818, 1995.
- Li CL, Bak AF, Parker LO. Specific resistivity of the cerebral cortex and white matter. *Exp Neurol* 20: 544–557, 1968.
- Lopez-Agudo L, Ibarz JM, Herrerias O. Activity-dependent changes of tissue resistivity in the CA1 region in vivo are layer-specific: modulation of evoked potentials. *Neuroscience* 108: 249–262, 2001.
- Maldonado PE, Godecke I, Gray CM, Bonhoeffer T. Orientation selectivity in pinwheel centers in cat striate cortex. *Science* 276: 1551–1555, 1997.
- Marin-Padilla M. The pyramidal cell and its local-circuit interneurons: A hypothetical unit of the mammalian cerebral cortex. *J Cogn Neurosci* 2: 180–194, 1990.
- McNaughton BL, O'Keefe J, Barnes CA. The stereotrode: a new technique for simultaneous isolation of several single units in the central nervous system from multiple unit records. *J Neurosci Methods* 8: 391–397, 1983.
- Mechler F, Ohiorhenuan IE, Victor JD. Speed dependence of tuning to one-dimensional features in V1. *J Neurophysiol* 97: 2423–2438, 2007.
- Mechler F, Victor JD. Dipole characterization of single neurons from their extracellular action potentials. *J Comput Neurosci* doi:10.1007/s10827-011-0341-0.
- Moffitt MA, McIntyre CC. Model-based analysis of cortical recording with silicon microelectrodes. *Clin Neurophysiol* 116: 2240–2250, 2005.
- Mountcastle VB. Introduction. Computation in cortical columns. *Cereb Cortex* 13: 2–4, 2003.
- Murakami S, Okada Y. Contributions of principal neocortical neurons to magnetoencephalography and electroencephalography signals. *J Physiol* 575: 925–936, 2006.
- Musial PG, Baker SN, Gerstein GL, King EA, Keating JG. Signal-to-noise ratio improvement in multiple electrode recording. *J Neurosci Methods* 115: 29–43, 2002.
- Ohiorhenuan IE, Mechler F, Purpura KP, Schmid AM, Hu Q, Victor JD. Sparse coding and high-order correlations in fine-scale cortical networks. *Nature* 466: 617–621, 2010.
- Ohki K, Chung S, Ch'ng YH, Kara P, Reid RC. Functional imaging with cellular resolution reveals precise micro-architecture in visual cortex. *Nature* 433: 597–603, 2005.
- Ohki K, Chung S, Kara P, Hubener M, Bonhoeffer T, Reid RC. Highly ordered arrangement of single neurons in orientation pinwheels. *Nature* 442: 925–928, 2006.
- O'Kusky J, Colonnier M. A laminar analysis of the number of neurons, glia, and synapses in the adult cortex (area 17) of adult macaque monkeys. *J Comp Neurol* 210: 278–290, 1982.
- Olshausen BA, Field DJ. How close are we to understanding v1? *Neural Comput* 17: 1665–1699, 2005.
- Pettersten KH, Einevoll GT. Amplitude variability and extracellular low-pass filtering of neuronal spikes. *Biophys J* 94: 784–802, 2008.
- Rall W. Electrophysiology of a dendritic neuron model. *Biophys J* 2: 145–167, 1962.
- Ranck JB Jr. Specific impedance of rabbit cerebral cortex. *Exp Neurol* 7: 144–152, 1963.

- Robinson DA.** Electrical properties of metal microelectrodes. *Proc IEEE* 56: 1065–1071, 1968.
- Rosenthal F, Woodbury JW, Patton HD.** Dipole characteristics of pyramidal cell activity in cat postcruciate cortex. *J Neurophysiol* 29: 612–625, 1966.
- Schmitzer-Torbert N, Jackson J, Henze D, Harris K, Redish AD.** Quantitative measures of cluster quality for use in extracellular recordings. *Neuroscience* 131: 1–11, 2005.
- Schneidman E, Berry MJ 2nd, Segev R, Bialek W.** Weak pairwise correlations imply strongly correlated network states in a neural population. *Nature* 440: 1007–1012, 2006.
- Seshagiri CV, Delgutte B.** Response properties of neighboring neurons in the auditory midbrain for pure-tone stimulation: a tetrode study. *J Neurophysiol* 98: 2058–2073, 2007.
- Sherwood CC, Lee PW, Rivara CB, Holloway RL, Gilissen EP, Simmons RM, Hakeem A, Allman JM, Erwin JM, Hof PR.** Evolution of specialized pyramidal neurons in primate visual and motor cortex. *Brain Behav Evol* 61: 28–44, 2003.
- Shlens J, Field GD, Gauthier JL, Grivich MI, Petrusca D, Sher A, Litke AM, Chichilnisky EJ.** The structure of multi-neuron firing patterns in primate retina. *J Neurosci* 26: 8254–8266, 2006.
- Sholl DA.** Dendritic organization in the neurons of the visual and motor cortices of the cat. *J Anat* 87: 387–406, 1953.
- Somogyvari Z, Zalanyi L, Ulbert I, Erdi P.** Model-based source localization of extracellular action potentials. *J Neurosci Methods* 147: 126–137, 2005.
- Tao L, Shelley M, McLaughlin D, Shapley R.** An egalitarian network model for the emergence of simple and complex cells in visual cortex. *Proc Natl Acad Sci USA* 101: 366–371, 2004.
- Victor JD, Mechler F, Repucci MA, Purpura KP, Sharpee T.** Responses of V1 neurons to two-dimensional hermite functions. *J Neurophysiol* 95: 379–400, 2006.
- Vigmond EJ, Perez Velazquez JL, Valiante TA, Bardakjian BL, Carlen PL.** Mechanisms of electrical coupling between pyramidal cells. *J Neurophysiol* 78: 3107–3116, 1997.
- Ward MP, Rajdev P, Ellison C, Irazoqui PP.** Toward a comparison of microelectrodes for acute and chronic recordings. *Brain Res* 1282: 183–200, 2009.
- Wolf MT, Burdick JW.** A Bayesian clustering method for tracking neural signals over successive intervals. *IEEE Trans Biomed Eng* 56: 2649–2659, 2009.
- Yao H, Li CY.** Clustered organization of neurons with similar extra-receptive field properties in the primary visual cortex. *Neuron* 35: 547–553, 2002.
- Yen SC, Baker J, Gray CM.** Heterogeneity in the responses of adjacent neurons to natural stimuli in cat striate cortex. *J Neurophysiol* 97: 1326–1341, 2007.
- Yoshimura Y, Dantzker JL, Callaway EM.** Excitatory cortical neurons form fine-scale functional networks. *Nature* 433: 868–873, 2005.
- Zhu W, Shelley M, Shapley R.** A neuronal network model of primary visual cortex explains spatial frequency selectivity. *J Comput Neurosci* 26: 271–287, 2009.

